HHS Public Access

Author manuscript

Nat Chem Biol. Author manuscript; available in PMC 2024 May 16.

Published in final edited form as:

Nat Chem Biol. 2023 April ; 19(4): 423–430. doi:10.1038/s41589-022-01208-y.

Insights into distinct signaling profiles of the μOR activated by diverse agonists

Qianhui Qu[1,2,9,#], **Weijiao Huang**[1,#], **Deniz Aydin**[1,2,5,8,#], **Joseph M. Paggi**[1,2,5,8,#], **Alpay B. Seven**[1,2,#], **Haoqing Wang**[1], **Soumen Chakraborty**[3,10], **Tao Che**[4,10], **Jeffrey F. DiBerto**[4], **Michael J. Robertson**[1,2], **Asuka Inoue**[6], **Carl-Mikael Suomivuori**[1,2,5,8], **Bryan L. Roth**[4,7], **Susruta Majumdar**[3,10], **Ron O. Dror**[1,2,5,8], **Brian K. Kobilka**[1], **Georgios Skiniotis**[1,2]

[1]Department of Molecular and Cellular Physiology, Stanford University School of Medicine, 279 Campus Drive, Stanford, California 94305, USA.

[2]Department of Structural Biology, Stanford University School of Medicine, 279 Campus Drive, Stanford, California 94305, USA.

[3]Center for Clinical Pharmacology, University of Health Sciences & Pharmacy at St. Louis and Washington University School of Medicine, St. Louis, MO 63131, USA.

[4]Department of Pharmacology, School of Medicine, University of North Carolina, Chapel Hill, NC 27599, USA

[5]Department of Computer Science, Stanford University, Stanford, California 94305, USA.

[6]Graduate School of Pharmaceutical Sciences, Tohoku University, Sendai, 980-8578, Japan

[7]Division of Chemical Biology and Medicinal Chemistry, Eshelman School of Pharmacy, University of North Carolina, Chapel Hill, NC 27599-7365, USA.

[8]Institute for Computational and Mathematical Engineering, Stanford University, Stanford, California, USA.

[9]Present address: Shanghai Stomatological Hospital, Fudan University and Shanghai Key Laboratory of Medical Epigenetics, International Co-laboratory of Medical Epigenetics and

Correspondence: susrutam@wustl.edu, ron.dror@stanford.edu, kobilka@stanford.edu, yiorgo@stanford.edu.
[#]These authors contributed equally

Author Contributions

W.H. and H.W. prepared protein samples for structural studies and conducted biochemical assays. Q.Q. and A.B.S collected and processed the cryo-EM data and generated the maps. Q.Q., M.J.R. and A.B.S. built and refined models. S.C synthesized MP. T.C. and J.F.D. performed signaling profile assays under the supervision of B.L.R. A.I. performed NanoBiT experiments. D.A. and J.M.P. performed and analyzed molecular dynamics simulations, with input from C.-M.S., under the supervision of R.O.D. Q.Q., W.H., D.A., J.M.P., A.B.S., S.M., R.O.D., B.K.K. and G.S. interpreted the data and wrote the manuscript with inputs from all authors. B.K.K. and G.S. supervised the project.

Competing interests

G.S. is a co-founder of and consultant for Deep Apple Therapeutics. B.K.K. is a co-founder of and consultant for ConfometRx. S.M. is a co-founder of Sparian biosciences. S.M. has filed a provisional patent on MP and related molecules.

Data and materials availability

The atomic coordinates for MP-μOR-Gi1 and LFT-μOR-Gi1-scFv complexes have been deposited in the Protein Data Bank with the accession codes 7T2G and 7T2H, respectively. The EM maps for MP-μOR-Gi1 and LFT-μOR-Gi1-scFv complexes have been deposited in EMDB with the accession codes EMD-25612 and EMD-25613, respectively. The composite non-model-based density modified map for MP-μOR-Gi1 is deposited to The Electron Microscopy Data Bank (EMDB) as the main map and used for model building. The locally refined individual maps are deposited as additional maps.

Metabolism (Ministry of Science and Technology), Institutes of Biomedical Sciences, Department of Systems Biology for Medicine, Fudan University, Shanghai 200032, China

[10]Department of Anesthesiology, Washington University School of Medicine, Saint Louis, MO 63110, USA

Abstract

Drugs targeting the μ-opioid receptor (μOR) are the most effective analgesics available but are also associated with fatal respiratory depression through a pathway that remains unclear. Here we investigated the mechanistic basis of action of lofentanil (LFT) and mitragynine pseudoindoxyl (MP), two μOR agonists with different safety profiles. LFT, one of the most lethal opioids, and MP, a kratom plant derivative with reduced respiratory depression in animal studies, exhibited markedly different efficacy profiles for G protein subtype activation and β-arrestin recruitment. Cryo-EM structures of μOR-Gi1 complex with MP (2.5Å) and LFT (3.2Å) revealed that the two ligands engage distinct sub-pockets, and molecular dynamics (MD) simulations showed additional differences in the binding site that promote distinct active-state conformations on the intracellular side of the receptor where G proteins and β-arrestins bind. These observations highlight how drugs engaging different parts of the μOR orthosteric pocket can lead to distinct signaling outcomes.

Introduction

Opioids targeting the μ-opioid receptor (μOR), such as the natural alkaloid morphine and synthetic agonists like fentanyl, remain the most effective analgesics for treating acute and chronic pain. The μOR is a G protein-coupled receptor (GPCR) that signals through six different heterotrimeric G protein subtypes: Gi1, Gi2, Gi3, GoA, GoB, and Gz (henceforth the Gi/o/z family) with varying efficacies and kinetics[1]. However, μOR activation can also recruit β-arrestins, which not only promote receptor endocytosis but also drive G protein-independent signaling.

Opioid receptor ligands range from small synthetic molecules to plant alkaloids and peptides with diverse scaffolds and distinct signaling properties[2]. Fentanyl and a series of congeners have been synthesized to initiate strong and rapid analgesia, and are commonly prescribed to treat chronic cancer pain or used in anesthesia management[3]. Although the pharmacology of these broadly used fentanyl compounds is well characterized, their detailed interaction network with the μOR has not been determined. Fentanyl analogues demonstrate an enhanced ability to desensitize μOR[4], and preferentially recruit β-arrestin-2 in PathHunter[5] as well as BRET based cellular assays[6]. LFT, in particular (Fig. 1a), is one of the most potent fentanyl analogues. At over 10,000 times more potent than morphine[7], LFT has an increased risk of addiction and overdose, and is therefore not used clinically.

On the other hand, kratom-derived MP is an indole-based analgesic alkaloid that is structurally different from the endogenous enkephalin-derived peptides, morphine derivatives, and synthetic analogs based on fentanyl (Fig. 1a). Kratom extract from the leaves of the tropical evergreen tree *Mitragyna speciosa* found in Southeast Asia has been used for centuries by local cultures to enhance endurance and combat fatigue. Recently, kratom has gained global popularity for its ability to relieve pain and alleviate symptoms

during opioid withdrawal, and it is also used recreationally with a claimed reduced addiction liability[8]. There are nearly 54 alkaloids present in kratom with mitragynine being the major alkaloid (~66% of total alkaloid content). It is currently believed that the μOR dependent oral analgesic actions of kratom are derived from the metabolism of mitragynine to 7-hydroxy mitragynine (7OH)[9]. Recent reports have also shown that MP is a minor metabolite of mitragynine[10]. Previously, we synthesized and systematically examined the pharmacological behaviors of a series of mitragynine-based natural products and analogs that included mitragynine, 7OH, and MP both *in vitro* and *in vivo*. We found that, mice treated with MP developed antinociceptive tolerance much more slowly compared with morphine, and that MP did not cause respiratory depression at doses that produce analgesia comparable to morphine at μOR[11].

The unwanted effects of opioids, including tolerance, constipation and respiratory depression, were previously attributed to μOR signaling through β-arrestins[12,13], fueling efforts to discover biased agonists that selectively stimulate G protein over arrestin[14–16]. However, a number of studies have raised doubts about the role of arrestin signaling in respiratory depression[17–19], and recent work argues for balanced agonists as a mechanism to circumvent tolerance mediated by opioids[20]. On the other hand, there are conflicting reports on the role of specific Gi/o/z subtypes in the actions of opioids *in vivo*. For instance, experiments using antisense RNA to reduce the expression of Gαi1, Gαi2 or Gαi3 showed an impaired supraspinal analgesic response to morphine only in mice treated with antisense RNA to Gαi2[21]. Of interest, analgesia produced by sufentanil in this study remained intact in mice treated with antisense RNA to Gαi2. However, these results conflict with other studies showing that supraspinal analgesia was intact in Gαi2 and Gαi3 knockout mice, whereas an impaired analgesic response to morphine was observed in heterozygous Gαo knockout mice[2]. In contrast, Gαz KO mice showed little or no change in the supraspinal analgesia of a single dose of morphine, yet there was a marked increase in analgesic tolerance, and a decrease in lethality where the LD_{50} (dose at which 50% of animals die) was 700 mg/kg for wildtype and greater than 800 mg/kg for homozygous Gαz knockout mice[22]. Notably, none of the studies above specifically examined respiratory depression, which is a frequent cause of morbidity and mortality among opioid users. It is thus currently unclear whether analgesia and/or respiratory depression may be mediated by more than one Gi/o/z subtype in an agonist specific manner.

To explore the molecular mechanisms contributing to μOR mediated respiratory depression, we examined the transducer coupling propensities along with the structural effects of LFT and MP, which differ in their *in vivo* potency and tendency to promote respiratory depression at equianalgesic doses. We observed that LFT and MP have distinct efficacy signaling profiles at Gi1, Gi2, Gi3, GoA, GoB and Gz, as well as their recruitment of β-arrestins. Structural analysis of the μOR-Gi1 complex bound to each of these ligands provides a glimpse into unique allosteric pathways that may contribute to these drugs' differential signaling profiles.

Results

Distinct signaling profiles for μOR activated by LFT and MP

Given the diametrically opposite attributes of LFT and MP for potency and safety in preclinical animal models, we performed a detailed comparison of their signaling profiles using the TRUPATH bioluminescence-resonance energy (BRET) platform[23] for Gi1, Gi2, Gi3, GoA, GoB and Gz activation, and a complimentary BRET-based β-arrestin-1 and -2 recruitment assay (Fig. 1b). The efficacies for MP and LFT were expressed as a percentage of the response to the reference ligand DAMGO, a peptide analog of the endogenous opioid met-enkephalin. DAMGO which had a narrow, ~2-fold potency spread with highest activity at Gz and lowest at Gi3, showed an observed potency rank order of Gz~Gi1>GoB~GoA>Gi2~Gi3 (Supplementary Table 1).

Compared to DAMGO, LFT promotes activation of all Gi/o/z proteins with higher efficacy at all subtypes, while arrestins are recruited to a comparable or greater level. The potency of activation of Gz was the highest, at more than nine times greater than activation of Gi3 and a potency rank order of Gz>Gi1>GoA~Gi2~Gi3>GoB. (Fig. 1b, Supplementary Table 1). In contrast, MP was a partial agonist at all Gi/o/z subtypes, with no detectable recruitment of β-arrestins. The potency of MP was similar for all six G protein subtypes with a potency spread of ~3-fold between Gz (0.9 nM) and GoB (3.2 nM); however, the efficacy at all Gi/o/z and arrestin subtypes was lower than DAMGO. Notably, the efficacy of MP against DAMGO and LFT as well as morphine at the three most abundant Gα-subtypes present in the brain (i.e., Gz, GoA, GoB and Gi1) was found to be significantly lower (Fig. 1b, Extended Data Figs. 1a–c). Another striking difference between MP and LFT is recruitment of β-arrestin-1 and β-arrestin-2, which is almost undetectable for MP in the BRET recruitment assay (Fig. 1b). The relative potencies and efficacies for Gi1, β-arrestin-1 and β-arrestin-2 were confirmed using Nano-BiT[1] enzyme complementation assays that monitored G protein dissociation and arrestin recruitment (Extended Data Fig. 1b), as well as GTPase-Glo™ assay (Promega) that measured GTP turnover (Extended Data Fig. 1c). As expected, LFT preferentially promoted the most efficacious β-arrestin-1 and -2 recruitment, while it was slightly more efficacious at Gi/o/z heterotrimer protein dissociation (Fig. 1c). In contrast, MP exhibited very little detectable activity towards recruitment of β-arrestins, and was as potent as DAMGO in G protein dissociation assays, consistent with the TRUPATH data (Fig. 1b) and previous characterization by GTPγS binding[11] and cAMP[24] assays.

Structures of μOR-Gi1 complex with MP or LFT

To probe the molecular basis of different signaling behaviors of μOR modulated by MP and LFT, we obtained cryo-EM structures of MP-μOR-Gi1 and LFT-μOR-Gi1-scFv complexes, as Gi1 is in the middle of the potency profiles for both MP and LFT (Fig. 1b). The map for LFT-μOR-Gi1-scFv was determined from holey carbon grids at a global nominal resolution of 3.2Å, whereas the map for MP-μOR-Gi1 was initially globally determined to 2.5Å, owing primarily to the use of holey gold grids that minimized specimen motion during data collection (Extended Data Figs. 2a–d). Notably, local refinement followed by density modification in Phenix, further improved the resolution of the map in several regions, revealing a number of well resolved water molecules (Figs. 2a, b, Extended Data Figs. 2

and Supplementary Fig. 1). The high-quality density maps enabled *de novo* modeling of ligands MP and LFT, and the atomic coordinates were further optimized using GemSpot[25] (Figs. 2a and 2b insets). The overall architectures of both MP-μOR-Gi1 and LFT-μOR-Gi1 are similar to the enkephalin-like agonist DAMGO-bound μOR-Gi1 structure[26] (Extended Data Fig. 3a). General structural hallmarks of GPCR activation, including the $DR^{3.50}Y$, $CW^{6.48}xP^{6.50}$, $P^{5.50}$-$I^{3.40}$-$F^{6.44}$ and $NP^{7.50}xxY^{7.53}$ motifs (superscripts denote generic Ballesteros–Weinstein numbering[27]) are essentially identical to that of DAMGO and morphinan agonist BU72[28], with the latter being co-crystallized with a G protein mimetic nanobody (Extended Data Figs. 3b–d). Also, very similar is the interface between nucleotide-free G protein and μOR in the MP, LFT and DAMGO structures, representing a canonical μOR-Gi1 coupling state (Extended Data Figs. 3e, f).

Notwithstanding the diverse structural scaffolds, both MP and LFT fit snugly in the same orthosteric site in the μOR composed of the extracellular side on transmembrane (TM) helices 2,3, 5, 6 and 7, which is also occupied by DAMGO, BU72 and the covalent antagonist βFNA[29] (Figs. 2c, d and Extended Data Fig. 4). The elongated LFT has an orientation similar to DAMGO and BU72, with the hydrophobic 1-phenethyl branch of LFT pointing towards a sub-pocket (sp1) formed by TM2–3 and ECL1–2, which is occupied by the bulky phenyl group of BU72 and the methyl-phenylalanine of DAMGO (Extended Data Fig. 4). In contrast, in addition to the central pocket (cp) shared by all ligands, MP occupies a novel sub-pocket (sp2) formed by TM1, TM2 and TM7, (Fig. 2d and Extended Data Fig. 4b). Of interest, the 9-methoxy group on the indole ring orients towards the spacious μOR extracellular outlet, which may explain the observation that various substituents on this indole C-9 position could retain similar affinity for the μOR[11]. We also note that considering the suboptimal fit of the β-methoxyacrylate tail of MP in the cryo-EM density, this moiety may interchangeably adopt two diametrically opposite orientations and both poses have been deposited to the PDB (Supplementary Fig. 1c).

The fentanyl derived synthetic compounds share a piperidinyl core and exhibit various *in vivo* potencies for the μOR, with fentanyl being approximately 80–100 times more potent than morphine in rodents[7]. Our LFT-bound μOR structure shows the placement of key functional groups shared by fentanyl derivatives that are not present in morphine. The aniline phenyl ring of LFT is sandwiched between $Y^{7.43}$ and $W^{6.48}$ in the central pocket; the 1-phenethyl group provides additional hydrophobic contacts with sp1 sub-pocket residues $W^{23.50}$, $V^{3.28}$, and $I^{3.29}$; and the carbomethoxy moiety is positioned midway between $Y^{3.33}$ and $W^{7.35}$ (Fig. 3b and Extended Data Fig. 4). The higher potency of fentanyl derivatives relative to morphine may be due to interactions with these additional sub-pockets of the μOR. Indeed, the morphinan agonist BU72 is also more potent than morphine, likely primarily owing to its extra phenyl ring inserted in the sp1 sub-pocket, as seen in the BU72-μOR crystal structure[28].

Addition of a carbomethoxy moiety onto the 4-axial position of the fentanyl piperidinyl group makes carfentanil approximately 100 times more potent than fentanyl (Extended Data Fig. 6a). To further probe the binding properties of fentanyl synthetics, we employed the Glide docking software[30] to predict the binding pose of fentanyl and carfentanil (see Methods). As expected, carfentanil's predicted binding pose was similar to LFT's binding

pose (Extended Data Fig. 6b). On the other hand, docking generated two high-scoring poses for fentanyl, the first in an orientation similar to that of LFT but with the terminal phenyl group positioned differently and the second in an orientation opposite to that of LFT. We employed molecular dynamics (MD) simulations to assess the stability of each potential fentanyl pose (Extended Data Fig. 6c-f). Fentanyl was stable in simulations initiated with a pose analogous to the cryo-EM pose of LFT. In simulations initiated with fentanyl in the first docked pose, fentanyl generally shifted to a pose analogous to the cryo-EM pose of LFT. In simulations initiated with fentanyl in the second docked pose, fentanyl was generally unstable, occasionally dissociating from the binding pocket entirely. Previous simulation studies, which employed enhanced sampling methods to examine the behavior of fentanyl when initially placed in a pose similar to our second docked pose, observed both ligand dissociation and a shift to a pose located deeper in the receptor[31]. Our results suggest that fentanyl predominantly adopts an LFT-like pose but cannot rule out other possibilities.

Ligand binding pocket interactions and dynamics

Closer inspection of the ligand binding network highlights a highly conserved salt-bridge interaction between μOR D147$^{3.32}$ and a protonatable amine (NH^+) of μOR ligands (Fig. 3 and Extended Data Fig. 4c). Previous μOR structures have shown that the phenol groups of both DAMGO and BU72 are positioned in the central pocket with their hydroxyl groups oriented to form a water mediated interaction with H297$^{6.52}$. Here we observe that LFT and MP position their aniline and carbomethoxy groups, respectively, deeper into the central pocket (Fig. 3, residues shown as grey sticks), forming extensive contacts with M151$^{3.36}$, W293$^{6.48}$, I296$^{6.51}$, I322$^{7.39}$ and Y326$^{7.43}$. In lieu of the phenolic hydroxyl group of DAMGO and morphinan ligands, LFT and MP position their N-propylamide and methoxyenolate moieties, respectively, in the TM5–6 region.

The side-chain of residue Q124$^{2.60}$ (blue stick, Fig. 3) separates sub-pockets sp1 and sp2 (represented by orange and yellow sticks, respectively, in Fig. 3) with a different side-chain orientation in the MP-bound structure, allowing space for the indole ring of MP (Fig. 3a). Using MD simulations, we found that when not sterically blocked, Q124$^{2.60}$ can form a hydrogen bond to Y326$^{7.43}$, stabilizing it in an inward position. In simulations with LFT, this interaction is nearly always present (Figs. 4a, b, Extended Data Fig. 6a and Supplementary Fig. 2). Interestingly, we found that DAMGO induces this interaction only part of the time. The difference in stability of this interaction for LFT and DAMGO can largely be explained by a difference in positioning of Y128$^{2.64}$. In simulations with LFT, Y128$^{2.64}$ forms an interaction with Q124$^{2.60}$, thereby stabilizing an interaction with Y326$^{7.43}$ (Figs. 4a, b, Extended Data Fig. 6a and Supplementary Fig. 2). However, this interaction forms less frequently in simulations with DAMGO, likely due to interference from the peptide backbone of the ligand. We found that a Q124$^{2.60}$A mutant reduces arrestin recruitment more than G protein signaling for both DAMGO and LFT (Supplementary Fig. 3). (The relative effect on G protein and arrestin pathways with MP could not be determined due to the lack of arrestin recruitment at the wild-type.) This supports the hypothesis that the Q124$^{2.60}$–Y326$^{7.43}$ interaction favors arrestin recruitment.

Characterization of the Q124$^{2.60}$A mutant also shows that the interaction between MP's indole ring and Q124$^{2.60}$ is critical for MP agonism, as the μOR Q124$^{2.60}$A mutant reduces the maximal Gi response by more than half and completely abolishes arrestin recruitment (Supplementary Fig. 3). In addition, the fact that the Q124$^{2.60}$A mutation reduces DAMGO's potency 100-fold indicates that the Q124$^{2.60}$ side chain contributes substantially to DAMGO's binding affinity.

These ligand-dependent differences in Q124$^{2.60}$–Y326$^{7.43}$ interactions, along with direct effects of the ligands on Y326$^{7.43}$, result in LFT favoring more counterclockwise rotations of TM7 (viewed from the extracellular side) when compared with MP. In simulations, stable π-π stacking is observed between LFT's aromatic aniline ring and Y326$^{7.43}$ (Fig. 4a, Extended Data Fig. 6b). Together with the strong Q124$^{2.60}$–Y326$^{7.43}$ interaction, this allows for more inward conformations of Y326$^{7.43}$ in LFT bound μOR (Fig. 4, Supplementary Fig. 2). The MP-bound structure shows a hydrogen-bond formed between Y326$^{7.43}$ and the indole amine (N1) of MP (Fig. 3a). The N1 is critical for MP activity as alkyl substitution reduces its receptor affinity[11]. In simulations, this hydrogen-bonding between Y326$^{7.43}$ and MP is less stable than LFT's π-π interaction, as the direct hydrogen bond can be replaced by a water-mediated interaction. Even though the hydrogen bond between Y326$^{7.43}$ and DAMGO is also liable to be replaced by a water-mediated interaction, this direct hydrogen-bond interaction is more frequently observed with DAMGO than MP (Extended Data Fig. 6b). The Q124$^{2.60}$–Y326$^{7.43}$ interaction also takes place more frequently in the presence of DAMGO, compared to MP. These result in an intermediate positioning of Y326$^{7.43}$ in the presence of DAMGO. As described below, our simulations suggest that this rotation of TM7 near the ligand binding pocket influences the conformation of the receptor's intracellular surface. For DAMGO, the Q124A mutation would abolish the occasional hydrogen bond interaction with Y326, which may affect both efficacy and potency. Nevertheless, we cannot claim with confidence that the observed effects are necessarily due to the aforementioned hydrogen bond, and neither is it straightforward to deconvolute the role of Q124 in the efficacy versus potency for different ligands.

Allosteric effects of ligands on the transducer interface

It has been hypothesized that different ligands modulate the equilibrium among multiple conformations of μOR, which in turn favor signaling through different transducers[32]. For μOR, it was not previously known what these conformations are, nor how different ligands select between them. The structures reported here, along with our previous structure of μOR bound to DAMGO, illuminate differences in protein–ligand interactions for ligands with a range of distinct pharmacological profiles. However, by themselves, these structures do not reveal how different binding pocket conformations result in distinct intracellular conformations, likely because the presence of a G protein overwhelms the effect of the ligands on the conformation of the receptor.

To understand how differences in the ligands propagate to the intracellular transducer binding site, we performed atomistic simulations with the G protein removed. We initiated simulations of μOR bound to MP, LFT, and DAMGO from the structures presented in this manuscript and the previously published DAMGO-bound μOR structure[26], respectively.

We hypothesized that in the absence of a G protein, the receptor would relax away from the G protein–bound state observed in the cryo-EM structures, revealing ligand-dependent differences in the conformational ensemble of the receptor.

The simulations showed two major conformational states of the intracellular coupling site that differ in TM7 (Figs. 5a, b, Extended Data Fig. 7). One state, which we refer to as the “canonical active state”, is essentially identical to the intracellular conformation observed in the G protein–bound cryo-EM structures. The other state, which we refer to as the “alternative state”, differs in that that the intracellular portion of TM7 is rotated counterclockwise (viewed from the extracellular side) and positioned inwards (towards TM3), and the kink in the NPxxY region is relaxed (Fig. 5, Extended Data Fig. 7). Notably, MP favors the canonical active state, LFT favors the alternative state, and DAMGO favors an equilibrium between these two states. These intracellular conformations may provide a link to the distinct transducer recruitment profiles reflected in our TRUPATH assays. For example, the narrower intracellular cavity observed in the alternative state due to the inward movement of TM7 might favor binding of certain arrestins, whereas the canonical active state might favor binding of certain G proteins.

The ligands control the occupancy of these two conformational states by favoring different rotations of TM7 (Figs. 5c, d). The formation of the hydrogen bond between Q124$^{2.60}$ and Y326$^{7.43}$ in the binding pocket, predominantly observed in the presence of LFT, increases the probability that the intracellular coupling site will adopt the alternative state (Extended Data Fig. 8). LFT is associated with a counterclockwise rotation of TM7, whereas MP is associated with a clockwise rotation of TM7. This rotation of TM7 is enabled by a change in the hydrogen bonding network in the sodium binding pocket. In the canonical active state, hydrogen bonds are present between N86$^{1.50}$–S329$^{7.46}$ and D114$^{2.50}$–N332$^{7.49}$. In the alternative state, these interactions are broken and replaced by hydrogen bonds between D114$^{2.50}$–S329$^{7.46}$ and D114$^{2.50}$–N150$^{3.35}$ (Extended Data Fig. 9).

MP and LFT favor intracellular μOR conformations that are similar to those observed at the angiotensin II type 1 receptor (AT_1R) for G-protein-biased and arrestin-biased ligands, respectively[33] (Extended Data Fig. 10a). For both μOR and AT_1R, the transition from the canonical active conformation to the alternative conformation involves a counterclockwise twist at TM7, leading to the inward movement of P333$^{7.50}$ and the shift of the hydrogen bonding network in the sodium binding pocket. The inward position of TM7 in the alternative conformation is farther from the inactive state for both receptors (Extended Data Fig. 10a). We also note that the alternative conformations of μOR and AT_1R differ in that the hinge region connecting TM7 to helix 8 is inwardly displaced in μOR, discouraging the downward Y336$^{7.53}$ rotamer observed at AT_1R (Extended Data Fig. 10b). This appears to be due to the interaction between R165$^{3.50}$ and two negatively charged residues at helix 8 (D340$^{8.47}$ and E341$^{8.48}$) that are unique to opioid receptors.

To validate the role of this ligand-stabilized rotation of TM7 in determining signaling behaviors, we characterized the signaling profile of MP, DAMGO, and LFT for the Y326$^{7.43}$F mutant. Since the loss of the hydroxyl group would disrupt the hydrogen bonds to Q124$^{2.60}$ and D147$^{3.32}$ (Fig. 4a), we hypothesized that this mutation would

favor outward conformations of Y326$^{7.43}$ and thereby promote a clockwise rotation of TM7, disproportionately reducing arrestin recruitment for all three ligands. Moreover, we hypothesized that this effect would be larger for MP and DAMGO than LFT because the mutation will disrupt the hydrogen bonds that MP and DAMGO form with Y326$^{7.43}$, but not the π-π stacking interaction that LFT forms with Y326$^{7.43}$. In accord with these hypotheses, the Y326$^{7.43}$F mutation eliminated detectable β-arrestin 2 recruitment for MP and reduced maximal β-arrestin 2 recruitment for DAMGO and LFT by 94% and 57%, respectively. The same mutation led to a lesser reduction in Gi activation, reducing maximal Gi1 activation for MP, DAMGO, and LFT by 68%, 36%, and 13%, respectively (Supplementary Fig. 3).

Discussion

The μOR, the endogenous enkephalin and β-endorphin receptor, is targeted by powerful pain medications with distinct scaffolds, such as morphine and fentanyl. Recent structures of the μOR bound to the morphinan antagonist βFNA, the morphinan agonist BU72 and the peptide agonist DAMGO, revealed how the orthosteric pocket can accommodate chemically diverse scaffolds. Here we provided high-resolution structural and mechanistic information for the kratom-derived metabolite agonist MP and fentanyl-like full-agonist LFT bound to the μOR in complex with Gi1. The hydrophobic nature of the orthosteric ligand binding site is responsible for the high-affinity of the predominantly hydrophobic LFT molecule, while a distinct sub-pocket is occupied solely by the MP scaffold. Our MD simulations provide novel insights into the plasticity of μOR activation and reveal how differences in ligand interactions within the orthosteric pocket can lead to different conformations of the intracellular G protein and β-arrestin coupling interface, resulting in marked differences in recruitment of β-arrestins and very distinct G protein activation profiles (Fig. 1b).

Recruitment of β-arrestins has long been postulated as a mechanism leading to adverse effects of opioid analgesics[13,34,35]. Using cell-based BRET assays, here we show that the lethal full agonist LFT triggers substantial β-arrestin binding compared to the agonist MP, potentially suggesting a correlation between biased signaling and side effects. However, LFT also substantially enhances G protein recruitment by μOR, and thus persistent activation of G proteins by LFT may also contribute to the unwanted effects. This would be in agreement with a proposed model whereby the lack of respiratory depression in several G protein biased μOR agonists can be attributed to partial agonism for G protein activation[17]. However, the different G protein activation profiles may also have a critical role in these effects. It has previously been shown that MP is approximately ten-fold more potent than morphine and produces the same level of analgesia, yet MP is much less efficacious in promoting respiratory depression than morphine[11]. Notably, the G protein signaling profile of morphine in cell-based BRET assays is comparable to that of DAMGO and LFT, but very different from MP (Supplementary Fig. 4). In these assays, morphine displayed the highest potency (1.25 nM) and efficacy (106%) at Gz and the lowest at Gi2 (6.1 nM) with a potency rank order of Gz~Gi1>GoB~Gi3>GoA~Gi2, while its efficacy at all Gα-subtypes was higher than MP (Extended Data Fig. 1a). These results suggest that the lower intrinsic efficacy at G protein subtype(s) for MP compared to LFT, DAMGO and morphine maybe an important parameter in dissociating analgesia from respiratory depression at equianalgesic doses. It must be noted that TRV130 (oliceridine) is also believed to be a partial agonist

and causes respiratory depression[36], however, it has only being characterized at the Gi-2 subtype, raising the possibility that higher efficacy at other subtypes could be responsible for its response, though other downstream signaling mechanisms downstream cannot be ruled out. Taken together, our findings emphasize the importance of a more complete functional characterization of μOR agonists for activation of all relevant G protein subtypes, as well as β-arrestin

Online Methods

Expression and purification of μOR

A modified *M. musculus* (GenBank: AAB60673.1) μOR construct with removable N-terminal Flag-tag and C-terminal 10X histidine tag was used in this study. N-terminal residues (1–63) of μOR were replaced with the thermostabilized apocytochrome b_{562}RIL from *Escherichia coli* (M7W, H102I and R106L) (BRIL) protein and a linker sequence (GSPGARSAS). N-terminal Flag-tag and C-terminal histidine tag were removable with rhinovirus 3C protease. μOR was expressed and purified as previously described[28]. Briefly, sf9 cells (Expression System) was infected with baculovirus at a density of $4X10^6$ cells/mL and incubated for 60 hours at 27 °C. Cell membrane was solubilized in n-dodecyl-b-D-maltoside (DDM, Anatrace) and 3-[(3-Cholamidopropyl)-dimethylammonio]-1-propanesulphonate (CHAPS, Anatrace) and purified by Ni-NTA resin (Thermo Scientific). The elute was further purified by M1 anti-Flag immunoaffinity resin and changed to a final buffer comprised of 25 mM HEPES pH 7.4, 100 mM NaCl, 0.01% lauryl maltose neopentyl glycol (L-MNG, Anatrace) and 0.001% cholesterol hemisuccinate (CHS, Sigma) by size exclusion chromatography. The peak fractions were collected and concentrated to ~100 μM.

Assembly and purification of the LFT-μOR-Gi1-scFv16 and MP-μOR-Gi1 complexes

The heterotrimeric Gi1 (Gαi1/Gβ2/Gγ1) and scFv16 was expressed and purified as previously described[26]. Briefly, the heterotrimeric Gi was expressed in Trichuplusia ni Hi5 cells and purified in a final buffer containing 20 mM HEPES pH 7.4, 100 mM NaCl, 0.05% DDM, 1 mM $MgCl_2$, 10 μM GDP and concentrated to ~20 mg/mL for complexing. The scFv16 was expressed and secreted from Trichuplusia ni Hi5 and purified in a buffer containing 20 mM HEPES 7.4, 100 mM NaCl and was concentrated to ~80 mg/mL for final use. Before complexing with μOR, the purified Gi heterotrimer was exchanged to L-MNG by adding equal volume of 20 mM HEPES 7.5, 50 mM NaCl, 1% L-MNG, 0.1% CHS, 1 mM $MgCl_2$, 50 μM TCEP and 10 μM GDP at room temperature for 1 hour.

To prepare LFT bound μOR-Gi1 complex, the receptor was incubated with LFT at a final concentration of 1 mM at 4°C for 1 hour. Ligand-bound μOR was mixed with a 1.2 molar excess of heterotrimeric Gi1 and incubated at room temperature for 1 hour. Apyrase and λ-phosphatase (New England Biolabs) were added to the complex and incubated for another 1 hour at 4°C. The mixture was purified by M1 anti-Flag affinity chromatography to remove excess Gi1 protein and gradually change to a final buffer containing 20 mM HEPES 7.4, 100 mM NaCl, 0.0075% L-MNG, 0.001% CHS, 0.0025% glycol-diosgenin (GND, Anatrace), 250 nM lofentanil, 2 mM EDTA and 200 μg/mL Flag peptide. A 1.25

excess of scFv16 was added to the complex and incubated at room temperature for 1 hour. The LFT-μOR-Gi1-scFv16 complex was further purified by size exclusion chromatography on a Superdex 200 10/300 GL column (GE healthcare) in 20 mM HEPES 7.4, 100 mM NaCl, 0.00075% L-MNG, 0.0001% CHS, 0.00025% GDN and 250 nM LFT. Peak fractions were concentrated ~20 mg/mL for electron microscopy studies.

For MP-μOR-Gi1 complex assembly, 500 μM MP was added to purified μOR while 1% L-MNG was added to purified Gi1. Both mixtures were incubated on ice for 1 h. After that, MP-bound μOR was mixed with a 1.5 molar excess of Gi1 heterotrimer and extra TCEP was added to maintain 100 μM TCEP concentration. The coupling reaction was allowed to proceed for another 1 h on ice, followed by addition of apyrase to catalyze GDP hydrolysis. The reaction mixture was left on ice overnight to allow stable complex formation. After that, the complexing mixture was purified by M1 anti-Flag affinity chromatography and eluted in 20 mM HEPES pH 7.5, 100 mM NaCl, 0.003% L-MNG, 0.001% glyco-diosgenin (GDN), 0.0004% CHS, 10 μM MP, 5 mM EDTA and Flag peptide. After elution, 100 μM TCEP was added to provide a reducing environment. Finally, the μOR–Gi1 complex was purified by size exclusion chromatography on a Superdex 200 10/300 gel filtration column in 20 mM HEPES pH 7.5, 100 mM NaCl, 5 μM MP, 0.003% L-MNG and 0.001% GDN with 0.0004% CHS total. Peak fractions were concentrated to ~10 mg/mL for electron microscopy studies.

Cryo-EM sample preparation and image acquisition

The homogeneity of purified LFT-μOR-Gi1-scFv16 or MP-μOR-Gi1 complex was evaluated by negative stain EM. For cryo-EM preparation of LFT-μOR-Gi1-scFv16 complex, 3.5 μL sample with addition of 0.05% β-OG was directly applied to glow-discharged 200 mesh gold grids (Quantifoil R1.2/1.3) and vitrified using a FEI Vitrobot Mark IV (Thermo Fisher Scientific). Images were collected on a Titan Krios (SLAC/Stanford) operated at 300 keV at a nominal magnification of 130,000X using a Gatan K2 Summit direct electron detector in counting mode, corresponding to a pixel size of 1.06Å. Movie stacks were obtained with a defocus range of −1.0 to −2.0 μm, using SerialEM with a set of customized scripts enabling automated low-dose image acquisition. Each movie stack was recorded for a total of 8 seconds with 0.2s exposure per frame and exposure dose set to 7 electrons per pixel per second.

MP-μOR-Gi1 protein complex was vitrified in a manner similar to LFT-μOR-Gi1-scFv16 complex, except on a 300 mesh UltrAuFoil grid (Quantifoil R1.2/1.3) and imaged at a magnification of 165,000 (0.82 Å/pixel). Movie stacks with dose fractioned over 40 frames, were recorded with a dose rate of 1.4 e/Å^2 (6.27 e/pixel/second) using counting mode with a defocus range of −0.8~−1.8 μm for MP-μOR-Gi protein complex using SerialEM.

Cryo-EM data processing

Datasets for LFT-μOR-Gi1-scFv16 and MP-μOR-Gi1 complex was processed using CryoSPARC (v3.2)[37] and Relion (v3.1)[38] respectively. For both LFT-μOR-Gi1-scFv16 and MP-μOR-Gi1 complex, a total 1853 or 1931 image stacks were subjected to beam-induced motion correction using CryoSPARC patch motion correction algorithm and MotionCor2[39], respectively (Extended Data Fig. 2, Supplementary Fig. 1). Contrast transfer function

parameters for each micrograph were estimated from the exposure-weighted averages of all frames by CryoSPARC patch CTF algorithm and Gctf (v1.06)[40], implemented in Relion. Particles were autopicked using reference-based picking, extracted with a box size of 256 pixels, and subjected to several rounds of 2D classification to remove contaminants. Initial maps were generated using stochastic gradient descent-based *ab-initio* refinement in CryoSPARC and Relion. Selected particle sets were further cleaned with several rounds of 3D classification. The final dataset of 152,809 particles for LFT-μOR-Gi1-scFv16 was subjected to 3D non-uniform refinement after Ctf refinement, generating a 3.2Å map sharpened with CryoSPARC. The final dataset of 413,821 particles for MP-μOR-Gi1 was subjected to 3D auto-refinement after Bayesian polishing and Ctf refinement, which generated a 2.5Å map. Resolution of these maps were estimated internally in CryoSPARC and Relion by gold standard Fourier shell correlation using the 0.143 criterion. The MP-μOR-Gi1 map was further locally refined with finer angular sampling (0.9 degrees) using masks including only the receptor or G protein heterotrimer in Relion. Locally refined MP-μOR-Gi1 maps were density modified and sharpened with Resolve Cryo-EM procedure in Phenix (dev-4271) using non-model-based algorithms[41], which yielded improved local maps with better than 2Å resolution in stable areas (Extended Data Fig. 2, Supplementary Fig. 1). Composite maps for MP-μOR-Gi1 were generated using ChimeraX (v1.2)[42]. The composite non-model-based density modified map for MP-μOR-Gi1 is deposited to The Electron Microscopy Data Bank (EMDB) as the main map. The locally refined maps are deposited as additional maps. Local resolution estimation was performed with CryoSPARC's and Relion's own local resolution estimation algorithms using half maps.

Model building and refinement

Initial ligand models were generated by the Edit tool implemented in Phenix, using LFT or MP SMILES. Together with individual protein chains from the DAMGO-μOR-Gi1-scFv16 structure, all models were rigid-body docked into the corresponding cryo-EM density map in Chimera[43], followed by iterative manual adjustment in COOT[44] and real space refinement in Phenix. Ligand coordination was further optimized by GemSpot[25]. The model statistics were validated using Molprobity. Structural figures were prepared in Chimera (v1.15), ChimeraX (v1.2) or PyMOL (Schrödinger) (The PyMOL Molecular Graphics System, Version 2.0 Schrödinger, LLC.) (https://pymol.org/2/). The final refinement statistics are provided in Supplementary Table 2.

Generating fentanyl and carfentanil docking models

The LFT-μOR cryo-EM structure was prepared for docking by removal of the ligand, and by the addition of missing sidechain atoms and hydrogen bonding optimization with Schrödinger's Maestro protein preparation wizard (Schrödinger Release 2018–4: Maestro, Schrödinger, LLC, New York, NY, 2018). Glide extra precision (XP) docking[30] was executed on the prepared structure with fentanyl or carfentanil. Docking identified largely identical poses for carfentanil but two distinct high-scoring poses for fentanyl.

System setup for molecular dynamics simulations

We performed simulations of μOR bound to MP, LFT, DAMGO, and fentanyl. We initiated MP- and LFT-bound simulations from the MP-μOR-Gi1, and LFT-μOR-Gi1-scFv16

structures reported in this manuscript, respectively. We initiated the DAMGO-bound simulations from the previously published DAMGO-μOR-Gi1 structure (PDB ID: 6DDF)[26]. We initiated fentanyl-bound simulations from the LFT-μOR-Gi1-scFv16 structure reported in this manuscript and converted LFT to fentanyl using Maestro (Schrödinger Release 2018–4: Maestro, Schrödinger, LLC, New York, NY, 2018). We also initiated fentanyl-bound simulations from the top two unique docking poses of fentanyl. In all simulation conditions, we removed the Gi1 and scFv16 chains. For MP, LFT, and DAMGO simulations, we performed six independent simulations, each 3.5 μs in length. For fentanyl simulations, we performed ten independent simulations, each 1 μs in length. For each simulation, initial atom velocities were assigned randomly and independently.

For all simulation conditions, the protein structures were aligned to the Orientations of Proteins in Membranes entry for 5C1M (active μOR bound to BU72[28]) using PyMOL, and crystal waters from 5C1M were incorporated. Prime (Schrödinger)[45] was used to model missing side chains, and to add capping groups to protein chain termini. Parameters for MP, LFT and fentanyl were generated using the Paramchem webserver[46]. Parameters for DAMGO were obtained as previously described[26]. Protonation states of all titratable residues were assigned at pH 7, except for D114$^{2.50}$ and D164$^{3.49}$, which were protonated (neutral) in all simulations, as these conserved residues are reported to be protonated in the active states of several class A GPCRs[47,48]. Fixing these residues in the protonated state may have impacted our results, specifically the hydrogen bonding network analysis involving D114$^{2.50}$. Histidine residues were modeled as neutral, with a hydrogen atom bound to the epsilon nitrogen, as we did not find any cases where moving the hydrogen to the delta nitrogen would help optimize the local hydrogen-bonding network. Using Dabble[49], the prepared protein structures were inserted into a pre-equilibrated palmitoyl-oleoyl-phosphatidylcholine (POPC) bilayer, the system was solvated, and sodium and chloride ions were added to neutralize the system and to obtain a final concentration of 150 mM. The final systems comprised approximately 59,000 atoms, and system dimensions were approximately 80×80×90 Å.

Molecular dynamics simulation and analysis protocols

We used the CHARMM36m force field for proteins, the CHARMM36 force field for lipids and ions, and the TIP3P model for waters[50]. Simulations of the μOR bound to MP, LFT, and fentanyl were performed using the Compute Unified Device Architecture (CUDA) version of particle-mesh Ewald molecular dynamics (PMEMD) in AMBER20[51] on graphics processing units (GPUs). Simulations of the μOR bound to DAMGO were performed using AMBER18[52].

Systems were first minimized using three rounds of minimization, each consisting of 500 cycles of steepest descent followed by 500 cycles of conjugate gradient optimization. 10.0 and 5.0 kcal·mol^{-1}·Å^{-2} harmonic restraints were applied to protein, lipids, and ligand for the first and second rounds of minimization, respectively. 1 kcal·mol^{-1}·Å^{-2} harmonic restraints were applied to protein and ligand for the third round of minimization. Systems were then heated from 0 K to 100 K in the NVT ensemble over 12.5 ps and then from 100 K to 310 K in the NPT ensemble over 125 ps, using 10.0 kcal·mol^{-1}·Å^{-2} harmonic restraints applied

to protein and ligand heavy atoms. Subsequently, systems were equilibrated at 310 K and 1 bar in the NPT ensemble, with harmonic restraints on the protein and ligand non-hydrogen atoms tapered off by 1.0 kcal·mol^{-1}·Å^{-2} starting at 5.0 kcal·mol^{-1}·Å^{-2} in a stepwise fashion every 2 ns for 10 ns, and then by 0.1 kcal·mol^{-1}·Å^{-2} every 2 ns for 20 ns. Production simulations were performed without restraints at 310 K and 1 bar in the NPT ensemble using the Langevin thermostat and the Monte Carlo barostat, and using a timestep of 4.0 fs with hydrogen mass repartitioning. Bond lengths were constrained using the SHAKE algorithm[53]. Non-bonded interactions were cut off at 9.0 Å, and long-range electrostatic interactions were calculated using the particle-mesh Ewald (PME) method with an Ewald coefficient of approximately 0.31 Å, and 4th order B-splines. The PME grid size was chosen such that the width of a grid cell was approximately 1 Å. Trajectory frames were saved every 200 ps during the production simulations. The use of a 9.0 Å non-bonded interaction cutoff and a 4 fs timestep with hydrogen mass repartitioning may have affected the structural and kinetic properties of the lipid bilayer, potentially introducing artifacts in our simulations.

The AmberTools17 CPPTRAJ package was used to reimage trajectories[54]. The resulting trajectories were 1 ns per frame. Simulations were visualized and analyzed using Visual Molecular Dynamics (VMD)[55] and PyMOL.

The Y128$^{2.64}$–Q124$^{2.60}$ distance was measured between the side-chain oxygen of Y128$^{2.64}$ and the closer of the side-chain oxygen and nitrogen of Q124$^{2.60}$. The Y128$^{2.64}$–Q124$^{2.60}$ distance was measured between the side-chain oxygen of Y326$^{7.43}$ and the closer of the side-chain oxygen and nitrogen of Q124$^{2.60}$. The P333$^{7.50}$–L110$^{2.46}$ distance was measured between the Cα atoms of the two residues.

In Fig. 5d and Extended Data Fig. 11, intracellular TM7 rotation was calculated by first aligning each simulation frame to the DAMGO-μOR-Gi1 structure (PDB ID: 6DDF)[26], which was itself aligned to the OPM entry for 5C1M (BU72-μOR structure[28]) using backbone atoms in TM2, TM3, and TM5. Next, for each simulation frame, the difference vector between the XY positions (i.e. the projection onto the plane of the membrane) of the Cα atoms of pairs of consecutive residues was computed (see Extended Data Fig. 10a). The angle between these vectors in the simulation frame and the reference structure was computed for all four pairs of consecutive residues between N332$^{7.49}$ and Y336$^{7.53}$ (the NPxxY motif, a well-known conserved motif in class A GPCRs) and averaged.

In Figs. 4a and Extended Data Fig. 8, representative frames for each simulation condition were chosen such that the residue–residue and residue–ligand interactions formed match those formed in a majority of simulation frames under that condition. In Fig. 5 and Extended Data Figs. 12 and 13, simulation frames are representative of the different conformational states of the receptor as determined by the intracellular TM7 rotation metric.

To construct the probability distributions shown in Figs. 4b, 5d, and Extended Data Fig. 10b, we used trajectory frames from all simulations under each condition and applied a Gaussian kernel density estimator. Extended Data Fig. 15 shows histograms for the same distance metrics as in Fig. 4b and Extended Data Fig. 10b and demonstrates that the underlying distributions are well-behaved, justifying the use of the Gaussian kernel density estimator

(GKDE). We chose to show Gaussian kernel density estimates in the main text figures as they provide a clearer visual representation when overlaying multiple distributions in each plot. In Extended Data Fig. 9, we used GetContacts[56] to quantify the frequency of hydrogen bonds in the binding pocket, requiring the donor-to-acceptor distance to be less than 3.5 Å and the donor-hydrogen-acceptor angle larger than 110 degrees. Water-mediated hydrogen bonds are defined to occur if one water molecule forms hydrogen bonds with both residues simultaneously. We used a Tcl script (https://github.com/Jerkwin/gmxtools/tree/master/pipistack) to quantify the frequency of aromatic stacking interactions, requiring the distance between the aromatic centers to be less than 7 Å and the interplanar angle less than 45 degrees. We included the time series of the key distances, as well as the root-mean-square deviation (RMSD) of transmembrane helix backbone atoms to the initial cryo-EM structure, in Extended Data Fig. 16. The time series generally converge to stable distributions within 1 μs. To verify this conclusion, we used the self-consistency check criterion of the Lyman-Zuckerman method[57] in Extended Data Fig. 17. We compared the distributions of key distances during the second microsecond of each simulation (from 1 μs to 2 μs) with the corresponding distributions during the third microsecond (from 2 μs to 3 μs) and found that they match closely (Extended Data Fig. 17). For simulations of the μOR in complex with LFT, DAMGO, and MP, we discarded the first 1 μs of each simulation for all analyses to ensure that we use the most equilibrated parts of the simulations.

NanoBiT-β-arrestin recruitment assay

μOR-induced β-arrestin recruitment was measured by a NanoBiT-β-arrestin recruitment assay, in which interaction between μOR and β-arrestin was monitored by a NanoBiT enzyme complementation system. Human full-length β-arrestin1 and β-arrestin2 were N-terminally fused to a large fragment (LgBiT) of the NanoBiT luciferase with a 15-amino acid (GGSGGGGSGGGSSSGG) flexible linker (Lg-βarr1 and Lg-βarr2, respectively). Human full-length μOR (WT or mutants) was C-terminally fused to a small fragment (SmBiT) with the 15-amino acid flexible linker (μOR-Sm). Lg-βarr1, Lg-βarr2 and μOR-Sm constructs were inserted into a pCAGGS expression plasmid vector. HEK293A cells (Thermo Fisher Scientific) were seeded in a 10-cm culture dish at a concentration of 2×10^5 cells mL^{-1} (10 mL per dish in DMEM (Nissui Pharmaceutical) supplemented with 10% fetal bovine serum (Gibco), glutamine, penicillin and streptomycin) 1-day before transfection. Transfection solution was prepared by combining 20 μL (per dish, hereafter) of polyethylenimine solution (Polysciences; 1 mg/mL) and a plasmid mixture consisting of 500 ng Lg-βarr1 or Lg-βarr2 and 1 μg μOR-Sm in 1 mL of Opti-MEM (Thermo Fisher Scientific). After incubation for 1-day, transfected cells were harvested with 0.5 mM EDTA-containing Dulbecco's PBS, centrifuged and suspended in 10 mL of HBSS containing 0.01% bovine serum albumin (BSA; fatty acid–free grade; SERVA) and 5 mM HEPES (pH 7.4) (assay buffer). The cell suspension was dispensed in a white 96-well culture plate at a volume of 80 μL per well and loaded with 20 μL of 50 μM coelenterazine (Carbosynth; final concentration at 10 μM) diluted in the assay buffer. After 2-h incubation at room temperature, the plate was measured for baseline luminescence (Spectramax L, Molecular Devices) and 20 μL of 6X test compounds diluted in the assay buffer or the assay buffer alone (vehicle) were manually added. The plate was read for 15 min with an interval of 20 sec at room temperature. Luminescence counts recorded from 10 min to

15 min after compound addition were averaged and normalized to the initial counts. The fold-change signals were further normalized to the vehicle-treated signal and were plotted as a G protein dissociation response. The resulting luminescent counts were fitted to a four-parameter sigmoidal concentration-response curve using Prism 8 software (GraphPad Prism) and pEC_{50} values (negative logarithmic values of EC_{50} values) and E_{max} values ("Top" – "Bottom") were obtained from the curve fitting and used for calculation of mean and SEM. For individual experiments, we calculated E_{max}/EC_{50} of LFT or MP relative to that of DAMGO, a dimensionless parameter known as relative intrinsic activity (RAi) to indicate agonist activity, and used its base-10 log-transformed value (Log RAi) to obtain mean and SEM.

NanoBiT-G protein dissociation assay

μOR-induced Gi1 activation was measured by a NanoBiT-G protein dissociation assay, in which dissociation of Gαi1 subunit from Gβ1γ2 subunit was monitored by the NanoBiT system. Specifically, a NanoBiT-Gi1 protein consisting of LgBiT-containing $G\alpha_{i1}$ subunit (Lg-Gαi1), SmBiT-fused $G\gamma_2$ subunit harboring a C68S mutation (Sm-Gγ2 (C68S)) and untagged Gβ1 subunit was expressed in HEK293A cells together with a μOR construct harboring N-terminal HA signal sequence and FLAG-epitope tag and C-terminal GFP (FLAG-μOR-GFP). Cell seeding and transfection were performed in the same procedures as described in the NanoBiT-β-arrestin recruitment assay except for a plasmid mixture (500 ng Lg-Gαi1, 2.5 μg Gβ1, 2.5 μg Sm-Gγ2 (C68S) and 1 μg FLAG-μOR-GFP per 10-cm culture dish). After baseline luminescent measurement and addition of 20 μL test compounds, the plate was immediately placed in the luminescent microplate reader and measured for 5 min. Change in luminescent count from 3 min to 5 min was averaged and used to plot G-protein dissociation response. The G-protein dissociation signals were fitted to a four-parameter sigmoidal concentration-response curve and the Log RAi values were obtained as described above.

Flow cytometry analysis

HEK293 cells were seeded in a 12-well culture plate at a concentration of 2 × 105 cells/ml (1 ml per well) 1 day before transfection. The site-directed mutants were generated by QuikChange (Agilent) with corresponding oligonucleotide primers, and were verified by DNA sequencing of the full coding regions. Transfection solution was prepared by combining 2 μl of 1 mg/ml polyethylenimine solution and 500 ng of the plasmid encoding N-terminally FLAG-epitope-tagged μOR (WT or mutants) in 100 μl of Opti-MEM. One day after transfection, the cells were collected by adding 100 μl of 0.53 mM EDTA-containing D-PBS, followed by 100 μl of 5 mM HEPES (pH 7.4)-containing HBSS. The cell suspension was transferred in a 96-well V-bottom plate and fluorescently labelled by using anti-FLAG-epitope tag monoclonal antibody (Clone 1E6, Wako Pure Chemicals; 10 μg/ml diluted in 2% goat serum- and 2 mM EDTA-containing D-PBS (blocking buffer)) and a goat anti-mouse IgG secondary antibody conjugated with Alexa Fluor 647 (Thermo Fisher Scientific; 10 μg/ml in diluted in the blocking buffer). After washing with D-PBS, the cells were resuspended in 200 μl of 2 mM EDTA-containing-D-PBS and filtered through a 40-μm filter. Fluorescent intensity of single cells was quantified by an EC800 flow cytometer equipped with dual 488-nm and 642-nm lasers (Sony). Fluorescent signal derived from

Alexa Fluor 647 was recorded in a FL3 channel and flow cytometry data were analysed by a FlowJo software (FlowJo). Live cells were gated with a forward scatter ('FS-Peak-Lin') cutoff of 390 setting a gain value of 1.7 and samples were shown as a histogram with the FL3 channel (x axis). Values of mean fluorescence intensity from 20,000 cells per sample were used for statistical analysis.

Bioluminescence resonance energy transfer (BRET) assays

To measure μOR-mediated G protein dissociation of Gi1-, Gi2-, Gi3-, GoA-, GoB-, and Gz-containing heterotrimeric G proteins, HEK293T cells were co-transfected in a 1:1:1:1 ratio with human μOR and the optimal Gα-RLuc8, Gβ, and Gγ-GFP2 subunits described in the TRUPATH paper[23]. TransIT-2020 (Mirus Bio LLC) was used to complex the DNA at a ratio of 3 μL Transit per μg DNA, in Opti-MEM (Gibco-ThermoFisher) at a concentration of 10 ng DNA per μL Opti-MEM. After 16 hours, transfected cells were plated in poly-lysine coated 96-well white clear bottom cell culture plates in plating media (DMEM + 1% dialyzed FBS) at a density of 40–50,000 cells in 100 μL per well and incubated overnight. The next day, media was vacuum aspirated and cells were washed twice with 60 μL of assay buffer (20 mM HEPES, 1X HBSS, pH 7.4). Next, 60 μL of the RLuc substrate, coelenterazine 400a (Nanolight Technologies, 5 μM final concentration in assay buffer) was added per well, and incubated for 5 minutes to allow for substrate diffusion. Afterwards, 30 μL of drug (3X) in drug buffer (20 mM HEPES, 1X HBSS, 0.3% BSA, pH 7.4) was added per well and incubated for another 5 minutes. Plates were immediately read for both luminescence at 395nm and fluorescent GFP2 emission at 510 nm for 1 second per well using a Mithras LB940 multimode microplate reader. BRET ratios were computed as the ratio of the GFP2 emission to RLuc8 emission. Data were analyzed by a three-parameter nonlinear regression equation using Graphpad Prism 8 (Graphpad Software Inc., San Diego, CA). All experiments were repeated in at least three independent trials each with duplicate determinations.

To measure μOR recruitment of β-arrestin 1 and 2 subtypes, HEK293T cells were co-transfected in a 1:1:5 ratio with human μOR containing a C-terminal Renilla luciferase (RLuc8), human GRK2, and human β-arrestin1 or 2 containing an N-terminal mVenus. Each plate also contained wells co-transfected with pcDNA instead of mVenus-arrestin to measure background fluorescence. This assay was performed identically to the TRUPATH assay, except that the substrate used was coelenterazine h (Promega, 5 μM final concentration in drug buffer) and plates were read for luminescence at 485 nm and fluorescent mVenus emission at 530 nm. BRET ratios were computed as the ratio of the mVenus to RLuc8 emission, and the net BRET was calculated by background subtraction of the BRET ratio from pcDNA-transfected wells. Data were analyzed by a three-parameter nonlinear regression equation using Graphpad Prism 8. All experiments were repeated in at least three independent trials each with duplicate determinations.

Bias analysis was carried out using the method proposed by Kenakin et al[58] that is based on the Black and Leff operational method[59]. For this we followed the step-wise protocol described by Uprety et al recently[60].

GTPase Glo assay

The GTP turnover measurement was performed using the GTPase-Glo™ assay (Promega). The final reaction buffer consisted of 20 mM Hepes pH 7.5, 100 mM sodium chloride, 10 mM magnesium chloride, 50 uM TCEP, 0.01% LMNG/CHS, 20 μM GDP, 10 μM GTP. The receptors and G proteins were purified as described above. The reaction was initiated by incubating receptor (4 μM) in the presence of 80 μM agonist in buffer containing 20 mM HEPES pH 7.5, 100 mM sodium chloride, 10 mM magnesium chloride, 20 μM GTP, 0.01%LMNG/CHS. After incubation for 60 min at room temperature, G protein (2 μM) was added in buffer containing 20 mM HEPES pH 7.5, 100 mM sodium chloride, 10 mM magnesium chloride, 100 μM TCEP, 0.01%LMNG/CHS, and 40 μM GDP. After reaction, buffer containing GTPase-Glo reagent supplemented with 5 μM adenosine 5′-diphosphate (ADP) was added to the sample and the whole mixture was incubated for another 30 min at room temperature, to convert the remaining GTP into ATP. After the addition of detection reagent (Promega) and incubation for 10 min at room temperature, luminescence was measured using a Multimode Plate Reader (PerkinElmer). Data were normalized to DAMGO reference and analyzed using GraphPad Prism.

Extended Data

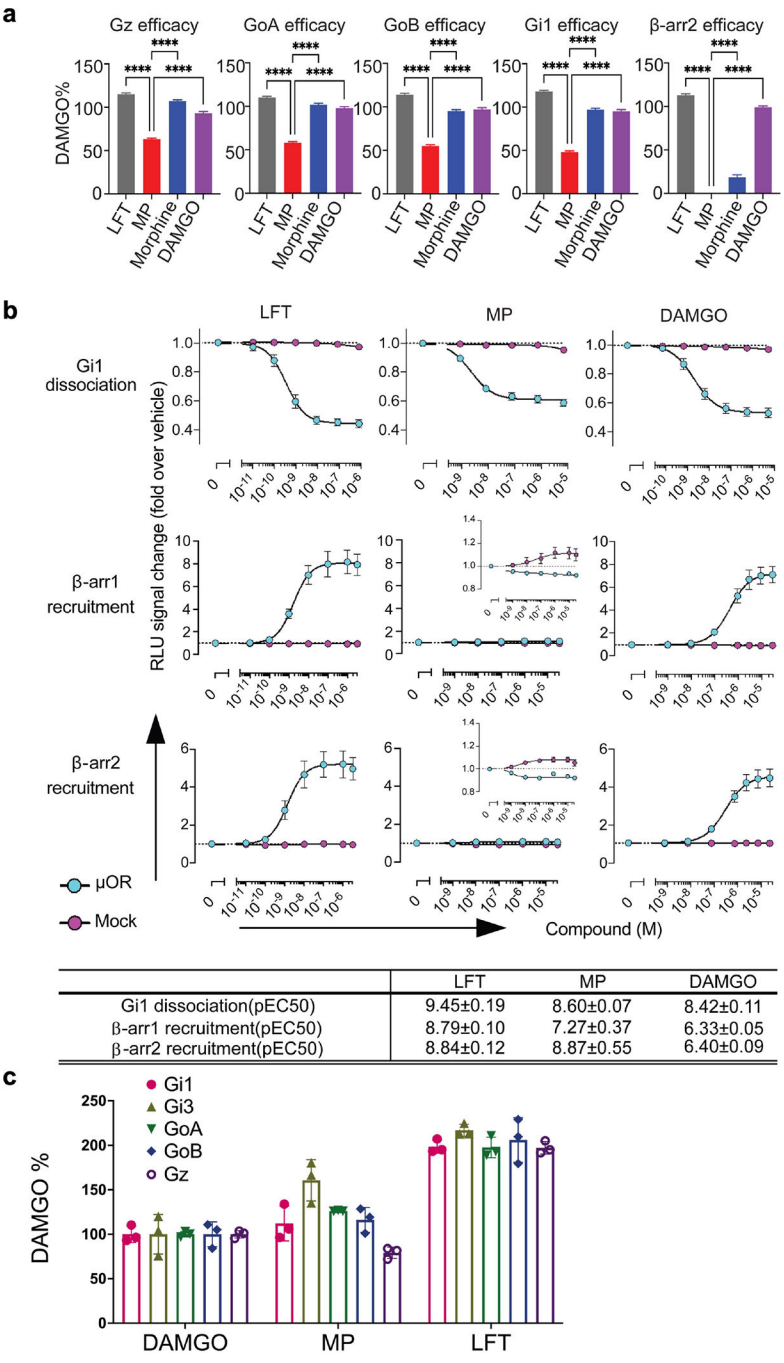

	LFT	MP	DAMGO
Gi1 dissociation(pEC50)	9.45±0.19	8.60±0.07	8.42±0.11
β-arr1 recruitment(pEC50)	8.79±0.10	7.27±0.37	6.33±0.05
β-arr2 recruitment(pEC50)	8.84±0.12	8.87±0.55	6.40±0.09

Extended Data Fig. 1 |. Activity characterization of diverse ligands on μOR.

a, Efficacy of compounds LFT, MP and Morphine at human μOR of Gi1, GoA, GoB and Gz activation, and recruitment of β-arrestin-2 using the BRET assay are shown as a percentage of receptor activation relative to the full agonist, DAMGO.MP had significantly lower G-protein as well as arrestin among ligands tested (****p<0.0001). Statistical significance was determined using one-way ANOVA followed by Dunnett's multiple comparison test.

Data represent mean + /− SEM from five independent experiments. **b,** Dose-dependent activation of Gi1 signaling in NanoBiT Gi1-dissociation assay and activation of β-arr1 and β-arr2 signaling in NanoBiT Arrestin-recruitment assay on wild type human μOR. Data are the means (+/− SEM) from four independent experiments and summarized at bottom panel. **c,** Efficacy of LFT, MP, and DAMGO at mouse μOR for Gi1, Gi3, GoA, GoB and Gz activation measured by GTPase-Glo™ assay (n = 3 independent replicates, means + /−SEM are represented).

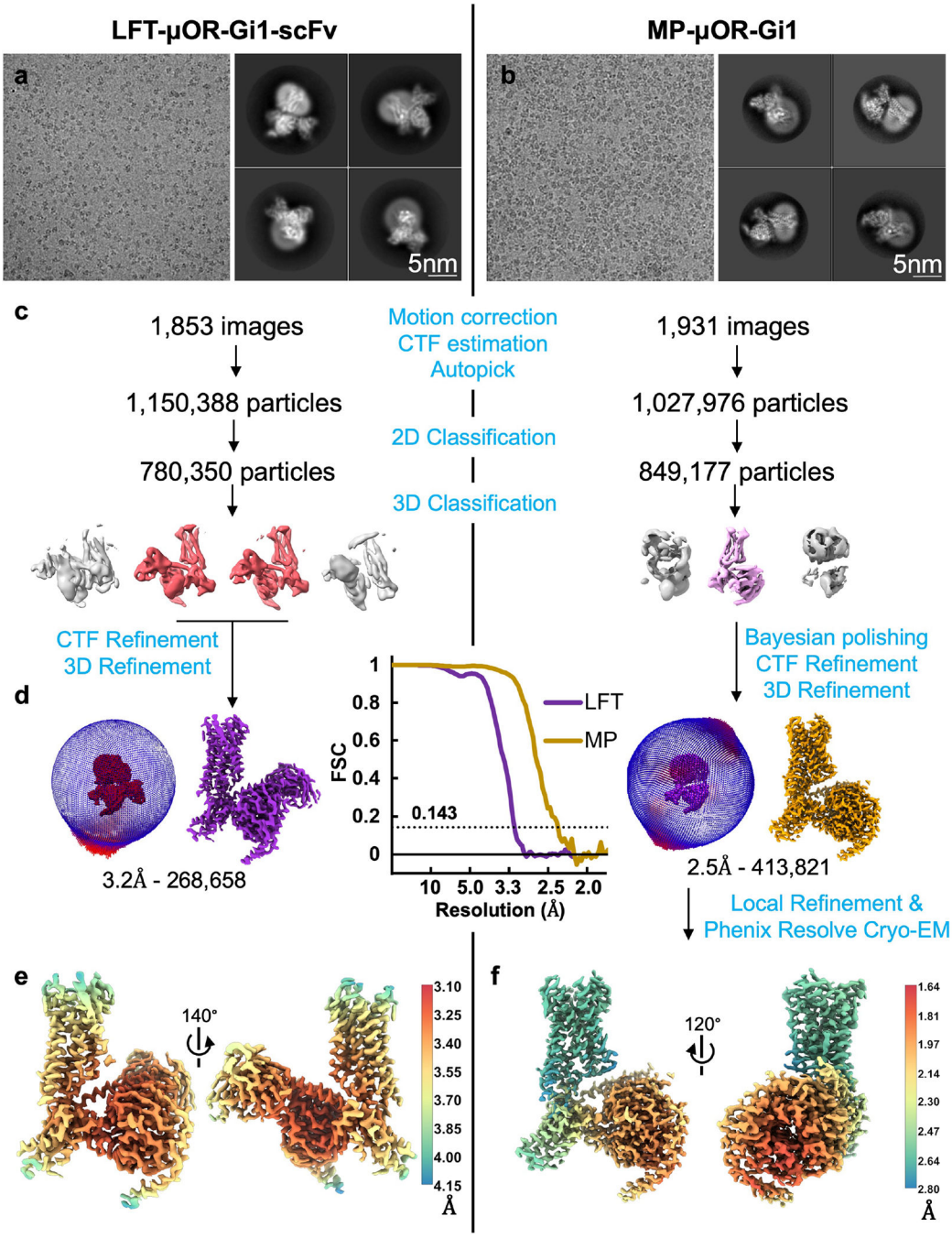

Extended Data Fig. 2 |. Cryo-EM process for LFT-μOR-Gi1-scFv and MP-μOR-Gi1 complexes. Representative raw micrographs (**a**) and 2D classification averages (**b**) for LFT-μOR-Gi1-scFv and MP-μOR-Gi1, respectively. **c,** Workflow of cryo-EM data processing of LFT (left) and MP (right). **d,** Angular distribution of projections for cryo-EM maps and gold-standard FSC curves of half-maps (0.143 cutoff). **e,** Local resolution of LFT-μOR-Gi1-scFv cryo-EM map. **f**, Local resolution of composite cryo-EM maps of MP-μOR-Gi1 after local refinement and non-model based density modification (Phenix Resolve Cryo-EM).

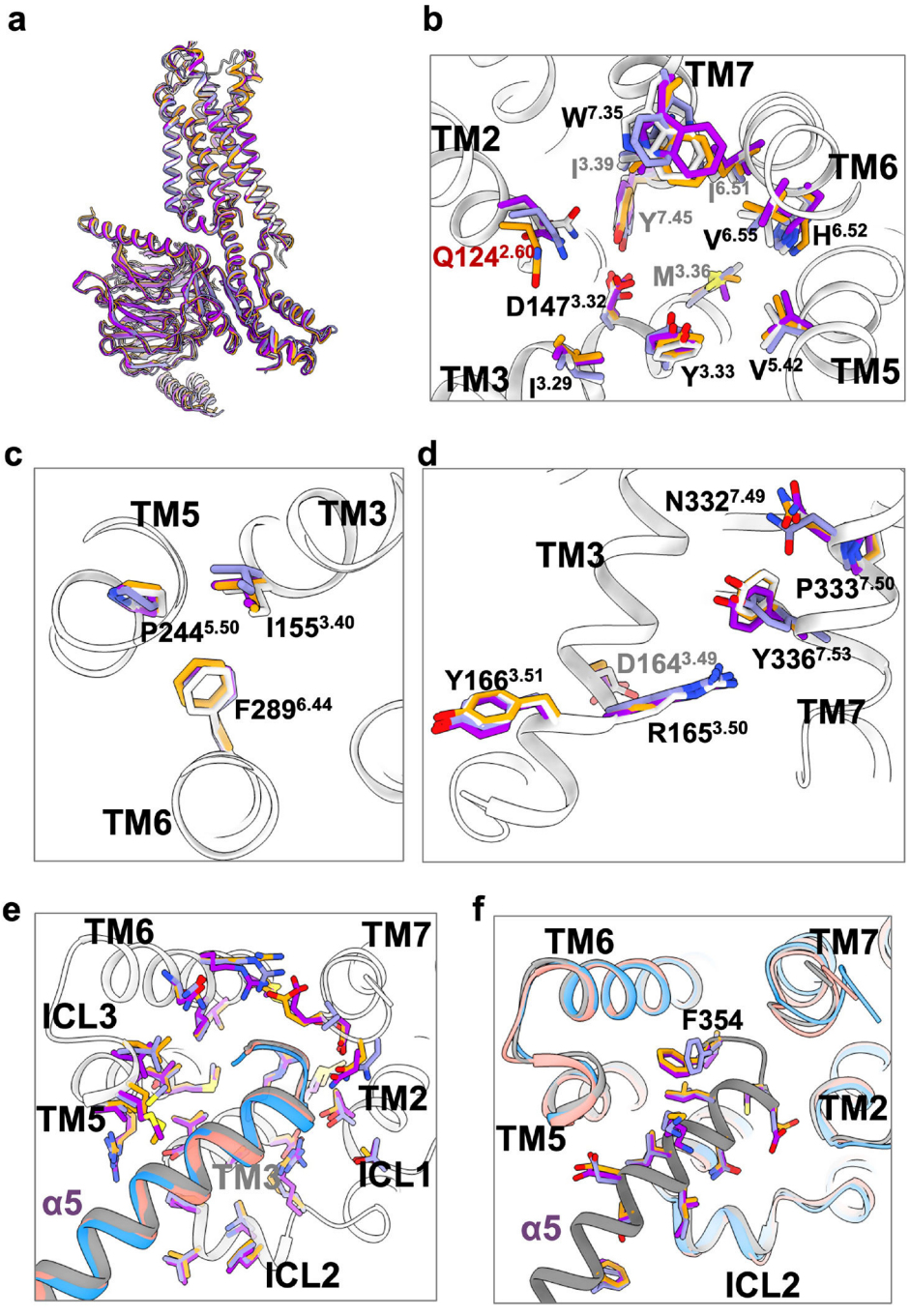

Extended Data Fig. 3 |. Conserved μOR-Gi1 conformation activated by diverse agonists.

a, Alignment of MP (orange), LFT (red) and DAMGO (blue) bound μOR-Gi1 complexes onto BU72-bound μOR (grey), with nanobody and scFv removed for clarity. **b,** Close view of the ligand binding orthosteric pocket show nearly identical poses for residues involved in different agonists interaction, except that Q214 orients its side-chain towards TM3 upon MP engagement, which results in the loss of Q214-Y326 interaction observed among LFT, DAMGO and BU72. Orientation of GPCR activation feature motifs $P^{5.50}$-$I^{3.40}$-$F^{6.44}$ (**c**), $DR^{3.50}Y$ and $NP^{7.50}xxY^{7.53}$ (**d**), and residues lined on the major interface between μOR intracellular site composed of TM2–3, TM5–7 and ICL1–3 (**e**) and C-terminal α5 helix of Gα subunit (**f**) are quite similar, suggesting a canonical conformation for Gi1 heterotrimer coupled μOR activated by DAMGO, LFT and MP.

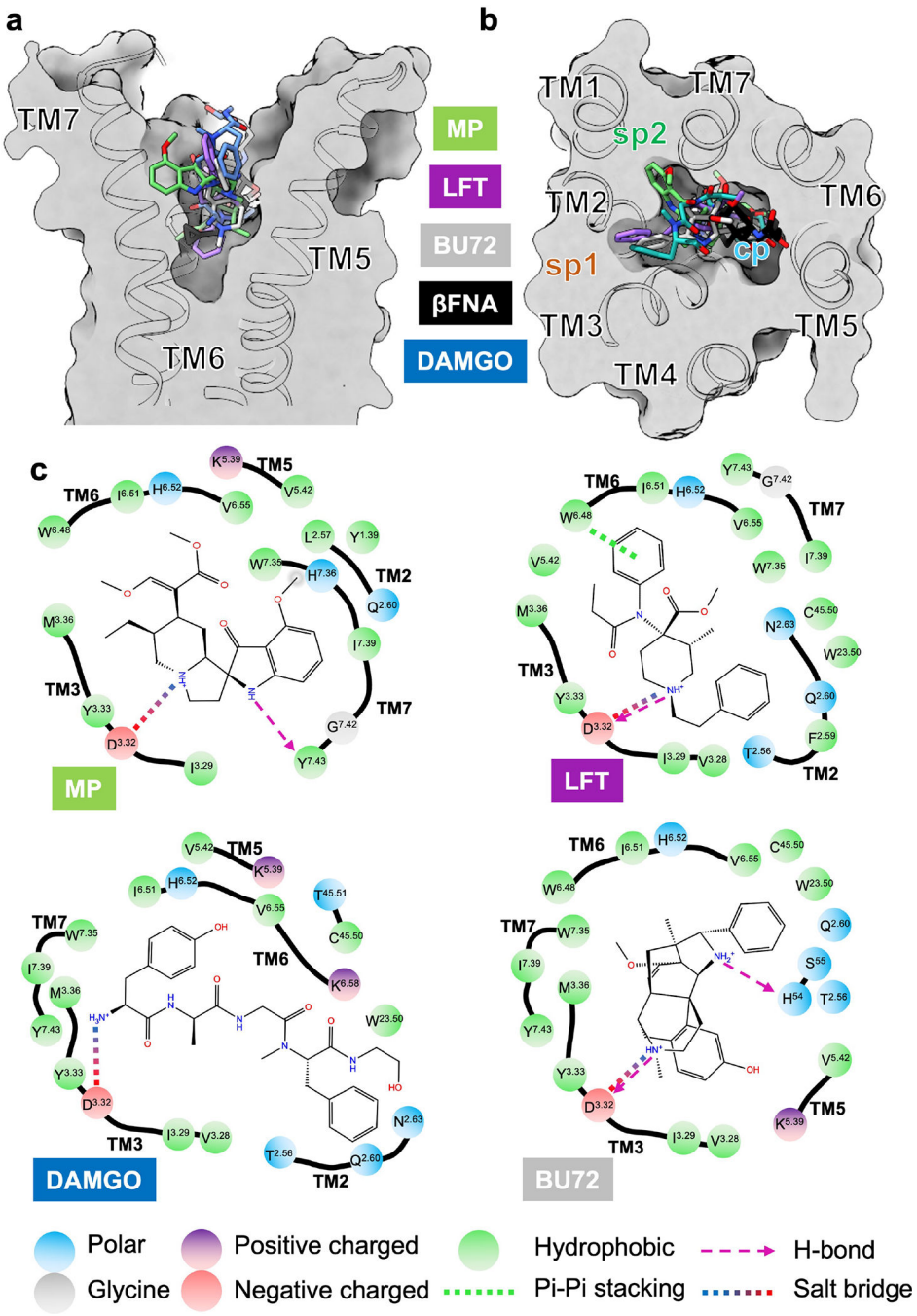

Extended Data Fig. 4 |. Interaction network comparison among diverse μOR ligands.

a, Structurally distinct agonists such as morphinan BU72 (grey), enkephalin-like DAMGO (blue), synthetic LFT (magenta), novel alkaloid MP (green) and morphinan antagonist βFNA (black) all occupy the central pocket (cp) of wide orthosteric binding site. **b**, Viewed from extracellular side, functional moieties of the BU72, DAMGO and LFT penetrate into a sub-pocket between TM2 and TM3 (sp1), while MP indole ring explores a new arena composed of TM1, TM2 and TM7 (sp2). **c,** Schematic interaction diagrams highlight a conserved salt-bridge/hydrogen-bond interaction between μOR D147 (red sphere) and

a tertiary amine (NH^+) on BU72, DAMGO, LFT and MP, in addition to the major hydrophobic interaction network, calculated by Maestro (Schrödinger Release 2018–4: Maestro, Schrödinger, LLC, New York, NY, 2018).

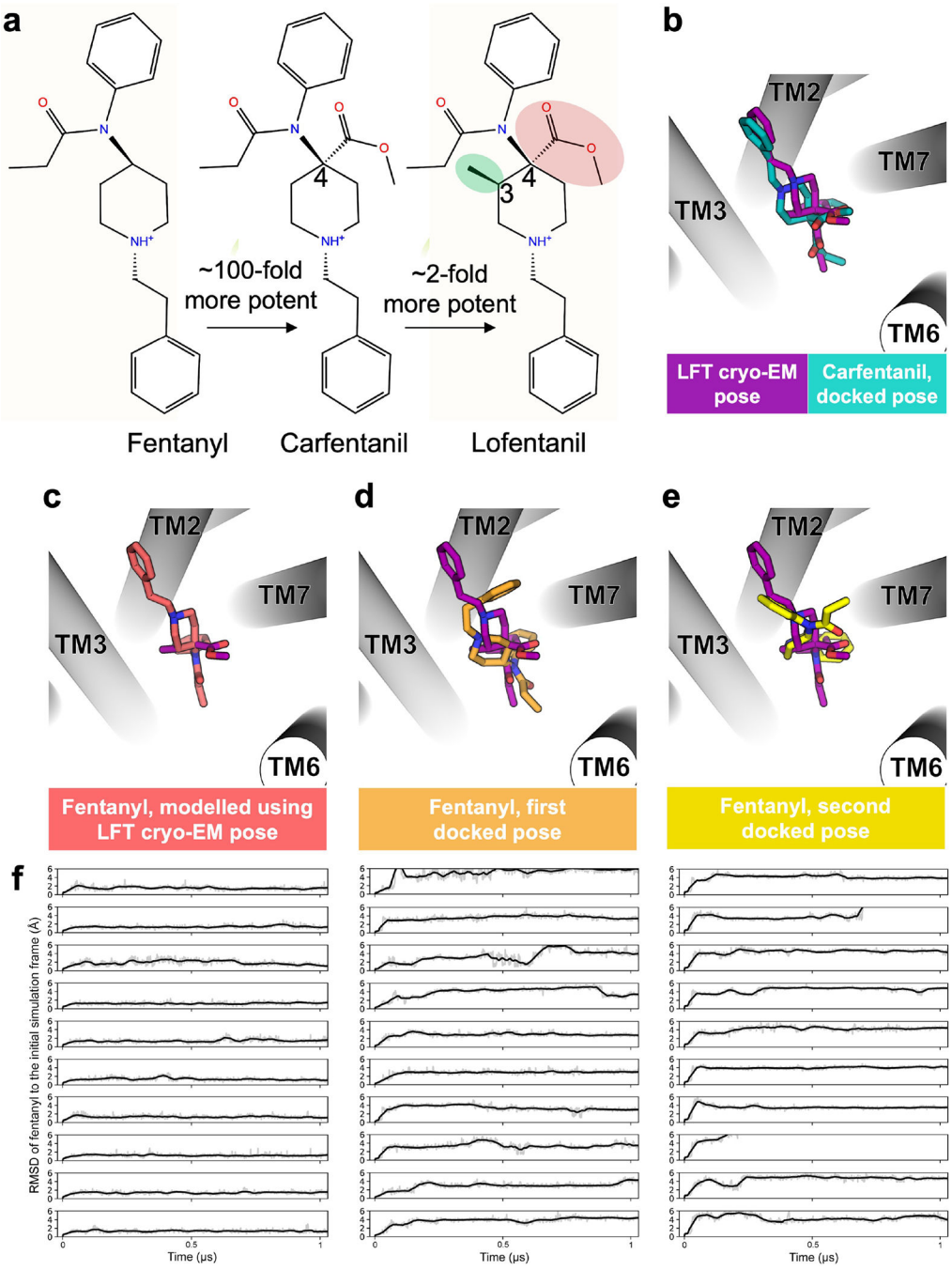

Extended Data Fig. 5 |. Binding poses of fentanyl analogues revealed by docking and simulation.
a, Chemical structures of fentanyl and its derivatives, carfentanil and lofentanil. The 4-carbomethoxy moiety added to the piperidinyl group of fentanyl makes carfentanil over 100 times more potent at the μOR, while further addition of the 3-methyl group slightly enhances

lofentanil in efficacy compared to carfentanil. **b-e,** Potential binding poses of carfentanil and fentanyl. The binding pose of LFT in the LFT-μOR cryo-EM structure (magenta sticks) is overlaid with (**b**) the docked pose of carfentanil (teal sticks), (**c**) the fentanyl pose modelled using the cryo-EM pose of LFT (pink sticks), (**d**) the first docked pose of fentanyl (orange stick), and (**e**) the second docked pose of fentanyl (yellow sticks). The first docked pose is in an orientation similar to that of LFT. The second docked pose is in an orientation opposite to that of LFT and has more favorable GlideScore and Emodel than the first. **f,** Simulations with fentanyl initiated in the poses of panels c, d, and e are shown in the first, second, and third columns, respectively (see Methods). For each simulation frame, the RMSD of fentanyl relative to the initial pose in that simulation is computed after alignment on the receptor. The first docked pose shifts to the pose shown in panel c in eight out of ten simulations.

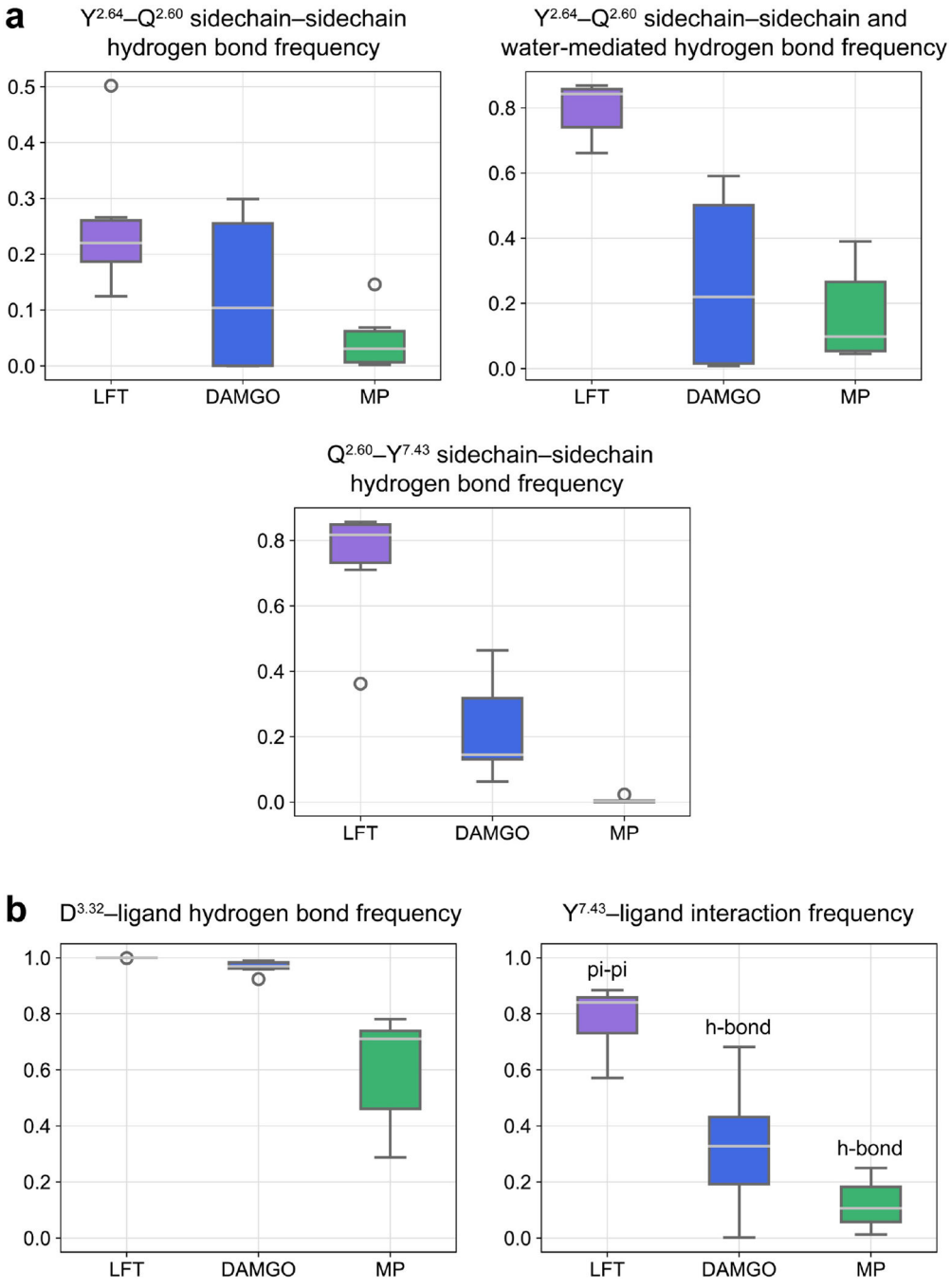

Extended Data Fig. 6 |. Frequencies of key interactions in the binding pocket with different ligands bound.

a, Frequency of key inter-residue hydrogen bonds in simulations with various ligands bound (see Methods). **b,** Frequency of key protein-ligand interactions in simulations with various ligands bound (see Methods). Lower and upper box boundaries indicate the 25th and 75th percentiles, respectively. The light gray line inside the box denotes the median. Lower and upper error lines represent 10th and 90th percentiles, respectively. Empty circles represent data points falling outside the 10th to 90th percentiles. Individual data points are frequencies

in each independent simulation. Each boxplot is computed over six independent simulations with the same ligand bound (see Methods).

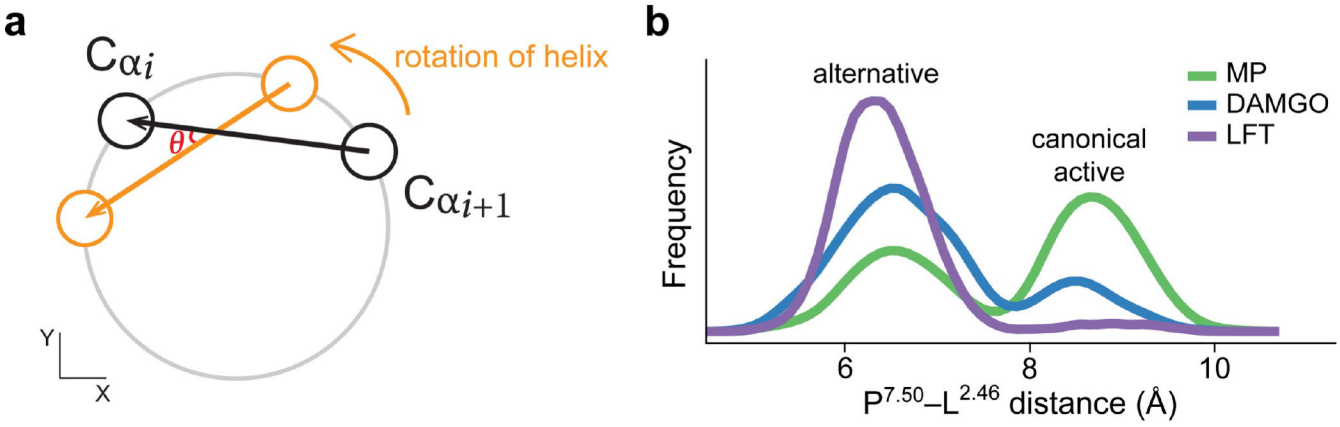

Extended Data Fig. 7 |. Intracellular TM7 rotation.

a, Intracellular TM7 rotation in Fig. 5d and Extended Data Fig. 11 was calculated as described in Methods. *i* and *i* + 1 denote consecutive residues. The view is from the extracellular side. The reference structure is represented in black, and the simulation frame is represented in orange. The computed angle is denoted by θ. **b,** The counterclockwise rotation in the intracellular portion of TM7 (when viewed from the extracellular side; see Fig. 5d) during the transition from the canonical active state to the alternative state leads to an inward shift as measured by a decrease in the $P^{7.50}$–$L^{2.46}$ distance. Relative to DAMGO, MP favors the canonical active state, whereas LFT favors the alternative state. Each distribution is computed over 6 independent simulations with the same ligand bound (see Methods).

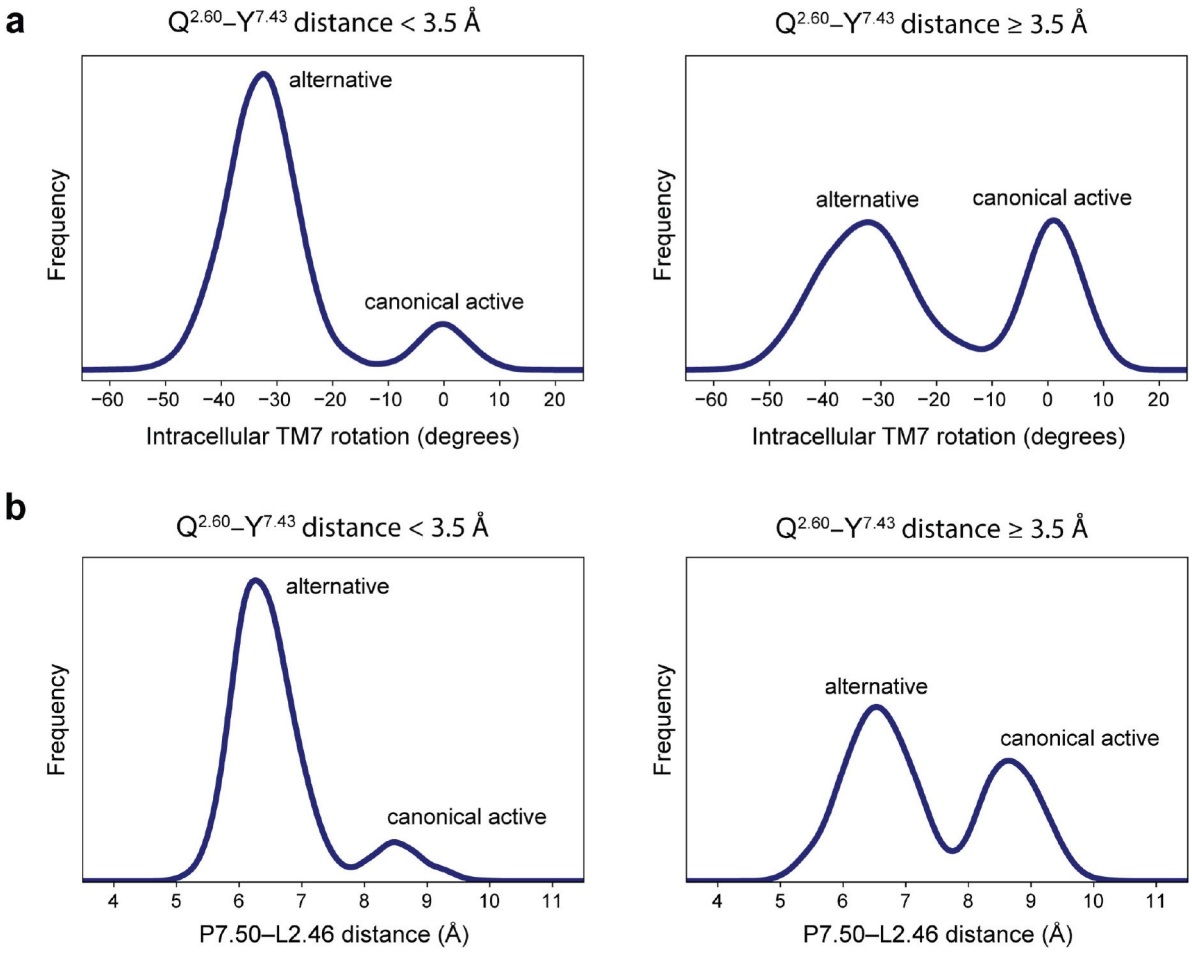

Extended Data Fig. 8 |. Interaction between Q2.60 and Y7.43 increases the probability that the intracellular coupling site adopts the alternative state conformation.

a,The distribution of intracellular TM7 rotation when the $Q^{2.60}$–$Y^{7.43}$ interaction is formed (left panel) and when it is not (right panel). **b,** The distribution of $P^{7.50}$–$L^{2.46}$ distance when $Q^{2.60}$–$Y^{7.43}$ interaction is formed (left panel) and when it is not (right panel). Distributions are computed across all 18 simulations (6 independent simulations with each of the 3 ligands bound; see Methods).

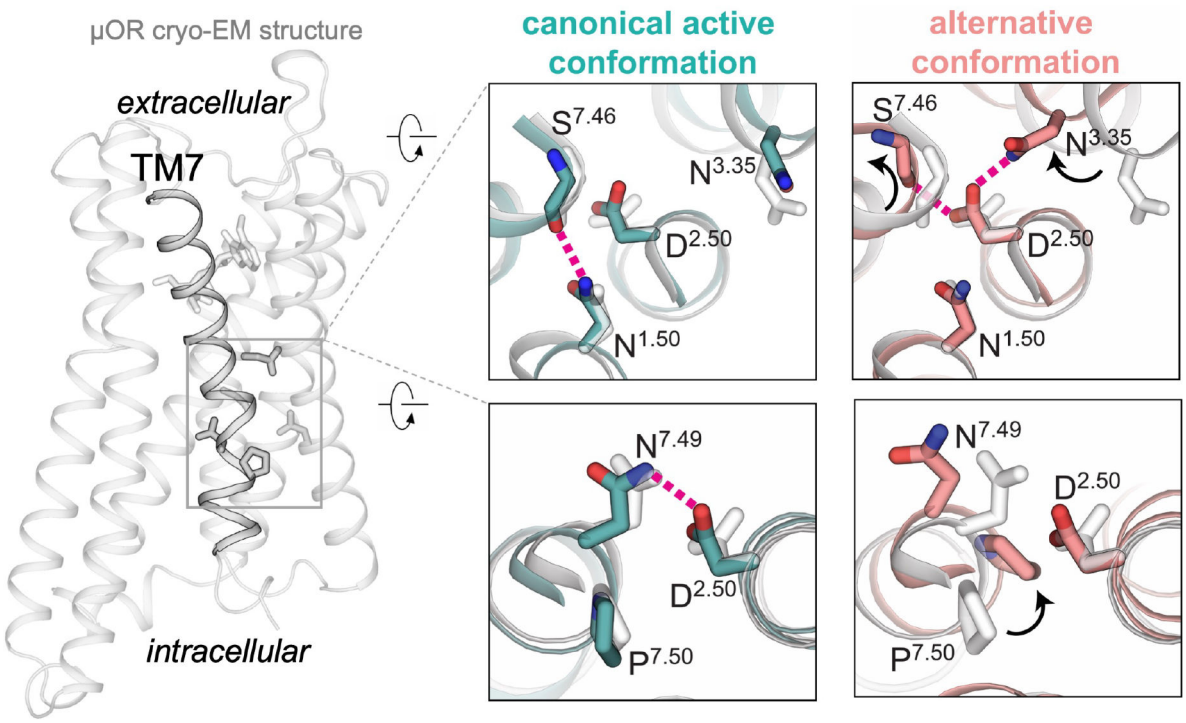

Extended Data Fig. 9 |. The transition from the canonical active conformation to the alternative conformation involves changes in an interaction network in the core of the receptor.

The transition from the canonical active conformation to the alternative conformation involves a shift in the hydrogen bonding network in the sodium binding pocket, as shown through representative frames from our μOR simulations. In the canonical active conformation, N86$^{1.50}$ forms a hydrogen bond with S329$^{7.46}$, and D114$^{2.50}$ forms a hydrogen bond with N332$^{7.49}$. In the alternative conformation, these interactions are broken and replaced by D114$^{2.50}$–S329$^{7.46}$ and D114$^{2.50}$–N150$^{3.35}$ hydrogen bonds. The μOR cryo-EM structure (grey) is represented by the MP-μOR-Gi1 structure reported in this manuscript.

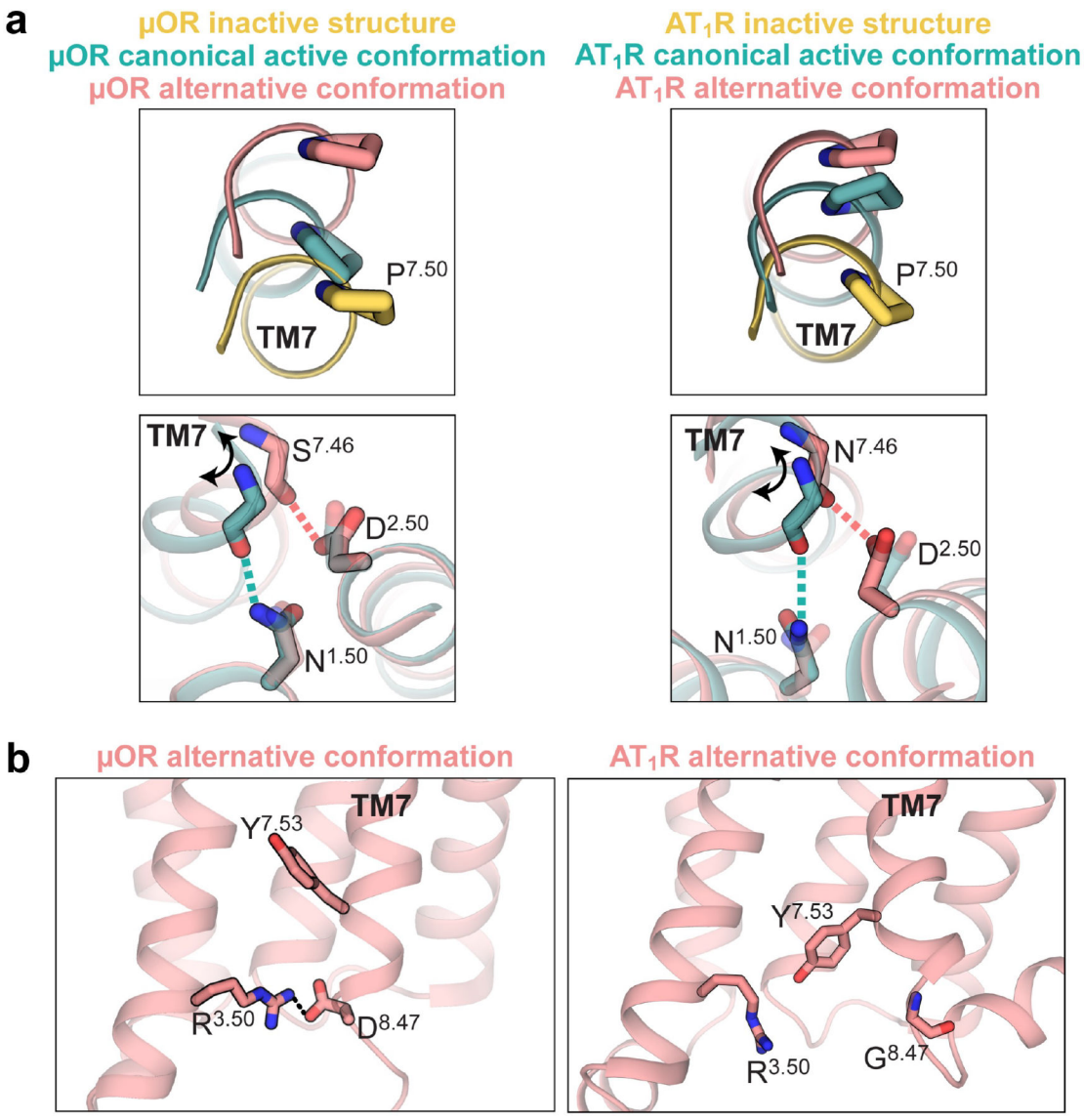

Extended Data Fig. 10 |. Comparison of the intracellular conformations observed for the μOR and the AT1R.

a, Simulations indicate that in both the μOR and the AT_1R, the transition from the canonical active conformation to the alternative conformation involves a counterclockwise twist at TM7 (bottom panels), leading to relaxation of the kink in the NPxxY region and the inward movement of $P^{7.50}$ (top panels). Both at the μOR and the AT_1R, $P^{7.50}$ is translated inward in the alternative conformation with respect to the canonical active conformation and the inactive conformation (top panels). **b**, The μOR alternative conformation differs from the AT1R alternative conformation in that the intracellular end of TM7 shows an inward displacement in μOR compared to the AT1R alternative conformation. The interaction between $R^{3.50}$ and $D^{8.47}$ does not allow the downward $Y^{7.53}$ rotamer observed at the AT1R. The canonical active and alternative conformations shown here for the μOR are representative frames from our μOR simulations (see Methods). The canonical active and alternative conformations shown here for the AT1R are representative simulation frames

(PDB files included in the Supplementary Material of Suomivuori, et al[34]. The inactive μOR and AT1R structures are the inactive μOR and AT1R crystal structures, respectively (PDB IDs: 4DKL and 4YAY).

Supplementary Material

Refer to Web version on PubMed Central for supplementary material.

Acknowledgements

This work was supported by the Swiss National Science Foundation Early Postdoctoral Mobility grant P2ELP3_187989 (D.A.), the European Molecular Biology Organization Long-Term Fellowship ALTF 544-2019 (D.A.), a Stanford Graduate Fellowship (J.M.P.), the Human Frontier Science Program Long-Term Fellowship LT000916/2018-L (C.-M.S.), the National Institutes of Health grants R01GM127359 (R.O.D.), DA045884 (S.M.), R37DA036246 (B.K.K. and G.S.) and the Mathers Foundation (G.S. and B.K.K.). B.K.K. is a Chan Zuckerberg Biohub Investigator. An award of computer time was provided by the INCITE program. This research used resources of the Oak Ridge Leadership Computing Facility, which is a U.S. Department of Energy Office of Science User Facility supported under contract DE-AC05-00OR22725. A.I. was funded by the PRIME 19gm5910013 (A.I.) and the LEAP 19gm0010004 and the BINDS JP20am0101095 from the Japan Agency for Medical Research and Development (AMED), KAKENHI 21H04791 and 21H05113 from the Japan Society for the Promotion of Science (JSPS), JST Moonshot Research and Development Program JPMJMS2023 from Japan Science and Technology Agency (JST). The authors thank Francois Marie Ngako Kadji, Kayo Sato, Yuko Sugamura and Ayumi Inoue at Tohoku University for plasmid construction and the cell-based GPCR assays; and Yianni Laloudakis, Scott Hollingsworth and Naomi Latorraca for helpful discussions.

Literature Cited

1. Masuho I et al. Distinct profiles of functional discrimination among G proteins determine the actions of G protein-coupled receptors. Sci Signal 8, ra123, doi:10.1126/scisignal.aab4068 (2015). [PubMed: 26628681]
2. Lamberts JT, Jutkiewicz EM, Mortensen RM & Traynor JR mu-Opioid receptor coupling to Galpha(o) plays an important role in opioid antinociception. Neuropsychopharmacology 36, 2041–2053, doi:10.1038/npp.2011.91 (2011). [PubMed: 21654736]
3. Stanley TH The history and development of the fentanyl series. J Pain Symptom Manage 7, S3–7, doi:10.1016/0885-3924(92)90047-l (1992). [PubMed: 1517629]
4. Bot G, Blake AD, Li S & Reisine T Fentanyl and its analogs desensitize the cloned mu opioid receptor. J. Pharmacol. Exp. Ther. 285, 1207–1218 (1998). [PubMed: 9618424]
5. Schmid CL et al. Bias factor and therapeutic window correlate to predict safer opioid analgesics. Cell 171, 1165–1175. e1113 (2017). [PubMed: 29149605]
6. Chakraborty S et al. A Novel Mitragynine Analog with Low-Efficacy Mu Opioid Receptor Agonism Displays Antinociception with Attenuated Adverse Effects. J Med Chem 64, 13873–13892, doi:10.1021/acs.jmedchem.1c01273 (2021). [PubMed: 34505767]
7. Meert TF, Lu HR, van Craenndonck H & Janssen PA Comparison between epidural fentanyl, sufentanil, carfentanil, lofentanil and alfentanil in the rat: analgesia and other in vivo effects. Eur J Anaesthesiol 5, 313–321 (1988). [PubMed: 2905988]
8. Prozialeck WC, Jivan JK & Andurkar SV Pharmacology of Kratom: An Emerging Botanical Agent With Stimulant, Analgesic and Opioid-Like Effects. J Am Osteopath Assoc 112, 792–799, doi:10.7556/jaoa.2012.112.12.792 (2012). [PubMed: 23212430]
9. Kruegel AC et al. 7-Hydroxymitragynine Is an Active Metabolite of Mitragynine and a Key Mediator of Its Analgesic Effects. ACS Cent Sci 5, 992–1001, doi:10.1021/acscentsci.9b00141 (2019). [PubMed: 31263758]
10. Kamble SH et al. Metabolism of a Kratom Alkaloid Metabolite in Human Plasma Increases Its Opioid Potency and Efficacy. ACS pharmacology & translational science 3, 1063–1068, doi:10.1021/acsptsci.0c00075 (2020). [PubMed: 33344889]

11. Varadi A et al. Mitragynine/Corynantheidine Pseudoindoxyls As Opioid Analgesics with Mu Agonism and Delta Antagonism, Which Do Not Recruit beta-Arrestin-2. J Med Chem 59, 8381–8397, doi:10.1021/acs.jmedchem.6b00748 (2016). [PubMed: 27556704]
12. Conibear AE & Kelly E A Biased View of μ-Opioid Receptors? Molecular Pharmacology 96, 542–549, doi:10.1124/mol.119.115956 (2019). [PubMed: 31175184]
13. Bohn LM, Gainetdinov RR, Lin FT, Lefkowitz RJ & Caron MG Mu-opioid receptor desensitization by beta-arrestin-2 determines morphine tolerance but not dependence. Nature 408, 720–723, doi:10.1038/35047086 (2000). [PubMed: 11130073]
14. Groer CE et al. An Opioid Agonist that Does Not Induce μ-Opioid Receptor—Arrestin Interactions or Receptor Internalization. Molecular pharmacology 71, 549–557, doi:10.1124/mol.106.028258 (2007). [PubMed: 17090705]
15. DeWire SM et al. A G Protein-Biased Ligand at the μ-Opioid Receptor Is Potently Analgesic with Reduced Gastrointestinal and Respiratory Dysfunction Compared with Morphine. Journal of Pharmacology and Experimental Therapeutics 344, 708–717, doi:10.1124/jpet.112.201616 (2013). [PubMed: 23300227]
16. Manglik A et al. Structure-based discovery of opioid analgesics with reduced side effects. Nature 537, 185–190, doi:10.1038/nature19112 (2016). [PubMed: 27533032]
17. Gillis A et al. Low intrinsic efficacy for G protein activation can explain the improved side effect profiles of new opioid agonists. Science Signaling 13, doi:10.1126/scisignal.aaz3140 (2020).
18. Bachmutsky I, Wei XP, Durand A & Yackle K ß-arrestin 2 germline knockout does not attenuate opioid respiratory depression. eLife 10, e62552 (2021). [PubMed: 34002697]
19. Kliewer A et al. Phosphorylation-deficient G-protein-biased μ-opioid receptors improve analgesia and diminish tolerance but worsen opioid side effects. Nature communications 10, 1–11 (2019).
20. He L et al. Pharmacological and genetic manipulations at the μ-opioid receptor reveal arrestin-3 engagement limits analgesic tolerance and does not exacerbate respiratory depression in mice. Neuropsychopharmacology, doi:10.1038/s41386-021-01054-x (2021).
21. Raffa RB, Martinez RP & Connelly CD G-protein antisense oligodeoxyribonucleotides and mu-opioid supraspinal antinociception. Eur J Pharmacol 258, R5–7, doi:10.1016/0014-2999(94)90073-6 (1994). [PubMed: 7925586]
22. Leck KJ et al. Deletion of guanine nucleotide binding protein alpha z subunit in mice induces a gene dose dependent tolerance to morphine. Neuropharmacology 46, 836–846, doi:10.1016/j.neuropharm.2003.11.024 (2004). [PubMed: 15033343]
23. Olsen RH et al. TRUPATH, an open-source biosensor platform for interrogating the GPCR transducerome. Nature chemical biology 16, 841–849 (2020). [PubMed: 32367019]
24. Zhou Y et al. Predicted Mode of Binding to and Allosteric Modulation of the mu-Opioid Receptor by Kratom's Alkaloids with Reported Antinociception In Vivo. Biochemistry 60, 1420–1429, doi:10.1021/acs.biochem.0c00658 (2021). [PubMed: 33274929]
25. Robertson MJ, van Zundert GC, Borrelli K & Skiniotis G GemSpot: a pipeline for robust modeling of ligands into cryo-EM Maps. Structure 28, 707–716. e703 (2020). [PubMed: 32413291]
26. Koehl A et al. Structure of the micro-opioid receptor-Gi protein complex. Nature 558, 547–552, doi:10.1038/s41586-018-0219-7 (2018). [PubMed: 29899455]
27. Ballesteros JA & Weinstein H Integrated methods for the construction of three-dimensional models and computational probing of structure-function relations in G protein-coupled receptors - ScienceDirect.
28. Huang W et al. Structural insights into μ-opioid receptor activation. Nature 524, 315–321 (2015). [PubMed: 26245379]
29. Manglik A et al. Crystal structure of the mu-opioid receptor bound to a morphinan antagonist. Nature 485, 321–326, doi:10.1038/nature10954 (2012). [PubMed: 22437502]
30. Friesner RA et al. Extra Precision Glide: Docking and Scoring Incorporating a Model of Hydrophobic Enclosure for Protein–Ligand Complexes. J. Med. Chem. 49, 6177–6196, doi:10.1021/jm051256o (2006). [PubMed: 17034125]
31. Mahinthichaichan P, Vo QN, Ellis CR & Shen J Kinetics and Mechanism of Fentanyl Dissociation from the μ-Opioid Receptor. JACS Au 1, 2208–2215, doi:10.1021/jacsau.1c00341 (2021). [PubMed: 34977892]

32. Wingler LM & Lefkowitz RJ Conformational Basis of G Protein-Coupled Receptor Signaling Versatility. Trends in cell biology 30, 736–747, doi:10.1016/j.tcb.2020.06.002 (2020). [PubMed: 32622699]
33. Suomivuori CM et al. Molecular mechanism of biased signaling in a prototypical G protein-coupled receptor. Science 367, 881–887, doi:10.1126/science.aaz0326 (2020). [PubMed: 32079767]
34. Grim TW, Acevedo-Canabal A & Bohn LM Toward Directing Opioid Receptor Signaling to Refine Opioid Therapeutics. Biological psychiatry 87, 15–21, doi:10.1016/j.biopsych.2019.10.020 (2020). [PubMed: 31806082]
35. Faouzi A, Varga BR & Majumdar S Biased Opioid Ligands. Molecules (Basel, Switzerland) 25, doi:10.3390/molecules25184257 (2020).
36. Gillis A et al. Low intrinsic efficacy for G protein activation can explain the improved side effect profiles of new opioid agonists. Sci Signal 13, doi:10.1126/scisignal.aaz3140 (2020).
37. Punjani A, Rubinstein JL, Fleet DJ & Brubaker MA cryoSPARC: algorithms for rapid unsupervised cryo-EM structure determination. Nat Methods 14, 290–296, doi:10.1038/nmeth.4169 (2017). [PubMed: 28165473]
38. Zivanov J et al. New tools for automated high-resolution cryo-EM structure determination in RELION-3. eLife 7, doi:10.7554/eLife.42166 (2018).
39. Zheng SQ et al. MotionCor2: anisotropic correction of beam-induced motion for improved cryo-electron microscopy. Nat Methods 14, 331–332, doi:10.1038/nmeth.4193 (2017). [PubMed: 28250466]
40. Zhang K Gctf: Real-time CTF determination and correction. J Struct Biol 193, 1–12, doi:10.1016/j.jsb.2015.11.003 (2016). [PubMed: 26592709]
41. Adams PD et al. PHENIX: a comprehensive Python-based system for macromolecular structure solution. Acta Crystallogr D Biol Crystallogr 66, 213–221, doi:10.1107/s0907444909052925 (2010). [PubMed: 20124702]
42. Goddard TD et al. UCSF ChimeraX: Meeting modern challenges in visualization and analysis. Protein Science : A Publication of the Protein Society 27, 14–25, doi:10.1002/pro.3235 (2018). [PubMed: 28710774]
43. Pettersen EF et al. UCSF Chimera--a visualization system for exploratory research and analysis. J Comput Chem 25, 1605–1612, doi:10.1002/jcc.20084 (2004). [PubMed: 15264254]
44. Emsley P, Lohkamp B, Scott WG & Cowtan K Features and development of Coot. Acta Crystallogr. D Biol. Crystallogr 66, 486–501, doi:10.1107/S0907444910007493 (2010). [PubMed: 20383002]
45. Jacobson MP, Friesner RA, Xiang Z & Honig B On the Role of the Crystal Environment in Determining Protein Side-chain Conformations. Journal of Molecular Biology 320, 597–608, doi:10.1016/S0022-2836(02)00470-9 (2002). [PubMed: 12096912]
46. Vanommeslaeghe K et al. CHARMM General Force Field (CGenFF): A force field for drug-like molecules compatible with the CHARMM all-atom additive biological force fields. Journal of computational chemistry 31, 671–690, doi:10.1002/jcc.21367 (2010). [PubMed: 19575467]
47. Ghanouni P et al. The effect of pH on beta(2) adrenoceptor function. Evidence for protonation-dependent activation. The Journal of biological chemistry 275, 3121–3127, doi:10.1074/jbc.275.5.3121 (2000). [PubMed: 10652295]
48. Mahalingam M, Martínez-Mayorga K, Brown MF & Vogel R Two protonation switches control rhodopsin activation in membranes. Proceedings of the National Academy of Sciences of the United States of America 105, 17795–17800, doi:10.1073/pnas.0804541105 (2008). [PubMed: 18997017]
49. Betz R Dabble 10.5281/zenodo.836914, 2017).
50. J, H. et al. CHARMM36m: an improved force field for folded and intrinsically disordered proteins. Nature Methods 14, 71–73, doi:10.1038/nmeth.4067 (2016). [PubMed: 27819658]
51. Case DA et al. Amber 2020: University of California, San Francisco. (2020).
52. Lee TS et al. GPU-Accelerated Molecular Dynamics and Free Energy Methods in Amber18: Performance Enhancements and New Features. J Chem Inf Model 58, 2043–2050, doi:10.1021/acs.jcim.8b00462 (2018). [PubMed: 30199633]

53. Ryckaert J-P, Ciccotti G & Berendsen HJC Numerical Integration of the Cartesian Equations of Motion of a System with Constraints: Molecular Dynamics of n-Alkanes. Journal of Computational Physics 23, 327–341, doi:10.1016/0021-9991(77)90098-5 (1977).
54. Roe DR & Cheatham TE PTRAJ and CPPTRAJ: Software for Processing and Analysis of Molecular Dynamics Trajectory Data. J. Chem. Theory Comput. 9, 3084–3095, doi:10.1021/ct400341p (2013). [PubMed: 26583988]
55. Humphrey W, Dalke A & Schulten K VMD: visual molecular dynamics. Journal of molecular graphics 14, 33–38, 27–38, doi:10.1016/0263-7855(96)00018-5 (1996). [PubMed: 8744570]
56. Venkatakrishnan AJ et al. Uncovering patterns of atomic interactions in static and dynamic structures of proteins. bioRxiv, 840694, doi:10.1101/840694 (2019).
57. Lyman E & Zuckerman DM Ensemble-based convergence analysis of biomolecular trajectories. Biophys J 91, 164–172, doi:10.1529/biophysj.106.082941 (2006). [PubMed: 16617086]
58. Kenakin T, Watson C, Muniz-Medina V, Christopoulos A & Novick S A simple method for quantifying functional selectivity and agonist bias. ACS Chem Neurosci 3, 193–203, doi:10.1021/cn200111m (2012). [PubMed: 22860188]
59. Black JW & Leff P Operational models of pharmacological agonism. Proceedings of the Royal Society of London. Series B, Biological sciences 220, 141–162, doi:10.1098/rspb.1983.0093 (1983). [PubMed: 6141562]
60. Uprety R et al. Controlling opioid receptor functional selectivity by targeting distinct subpockets of the orthosteric site. eLife 10, doi:10.7554/eLife.56519 (2021).

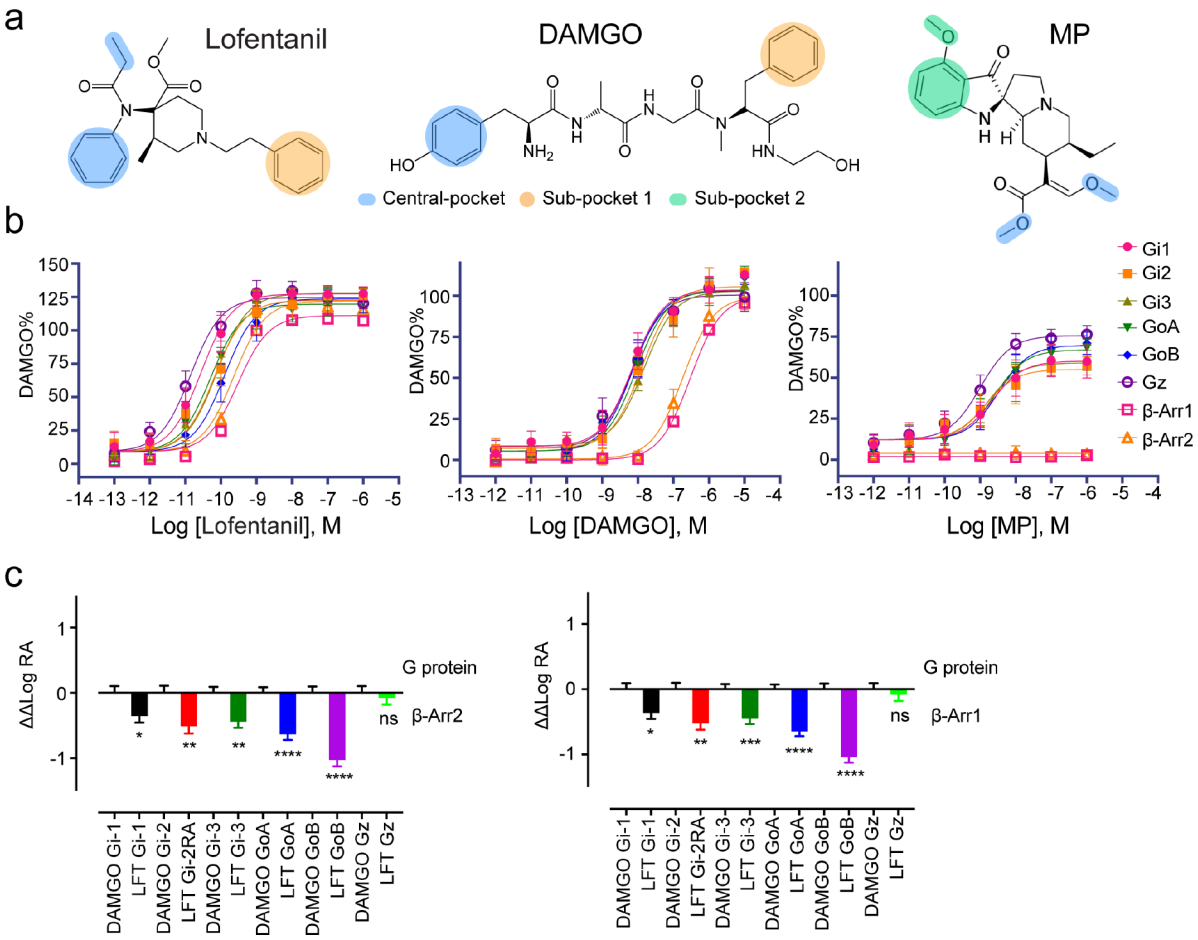

Fig. 1 |. Distinct ligands for μOR.

a, Structurally diverse μOR ligands with distinct pharmacological properties. Lofentanil; DAMGO, (D-Ala^2, N-MePhe^4, Gly-ol)-enkephalin; MP, Mitragynine pseudoindoxyl. **b,** Concentration-dependent activation of Gi1, Gi2, Gi3, GoA, GoB and Gz, and recruitment of β-arrestin-1 and β-arrestin-2 using BRET-based biosensors. Data for all functional assays that were carried out in hMOR were normalized to E_{max} of DAMGO (n=3 biological replicates, and data are presented as mean values +/− SEM). The dose response curves were fit using a three-parameter logistic equation in GraphPad Prism. **c,** Gi/o/z bias plots for LFT against β-arrestin2 (left) and β-arrestin1 (right) at hMOR using BRET assays. Bias analysis for signaling was performed as described in Methods. Data analyzed against DAMGO for LFT using unpaired t-test with Welch's correction. At β-arrestin2, LFT showed significant arrestin preference over Gi-1(*p=0.02), Gi-2(**p=0.003), Gi-3(**p=0.0025), GoA(****p<0.0001), GoB(****p<0.0001) while being a balanced agonist at Gz(ns, p=0.6). At β-arrestin1, LFT showed significant arrestin preference over Gi-1(*p=0.011), Gi-2(**p=0.001), Gi-3(***p=0.0007), GoA(****p<0.0001), GoB(****p<0.0001) while being a balanced agonist at Gz(ns, p=0.53). See also Extended Data Fig. 1 and Supplementary Table 1 for efficacy and potency data for ligands.

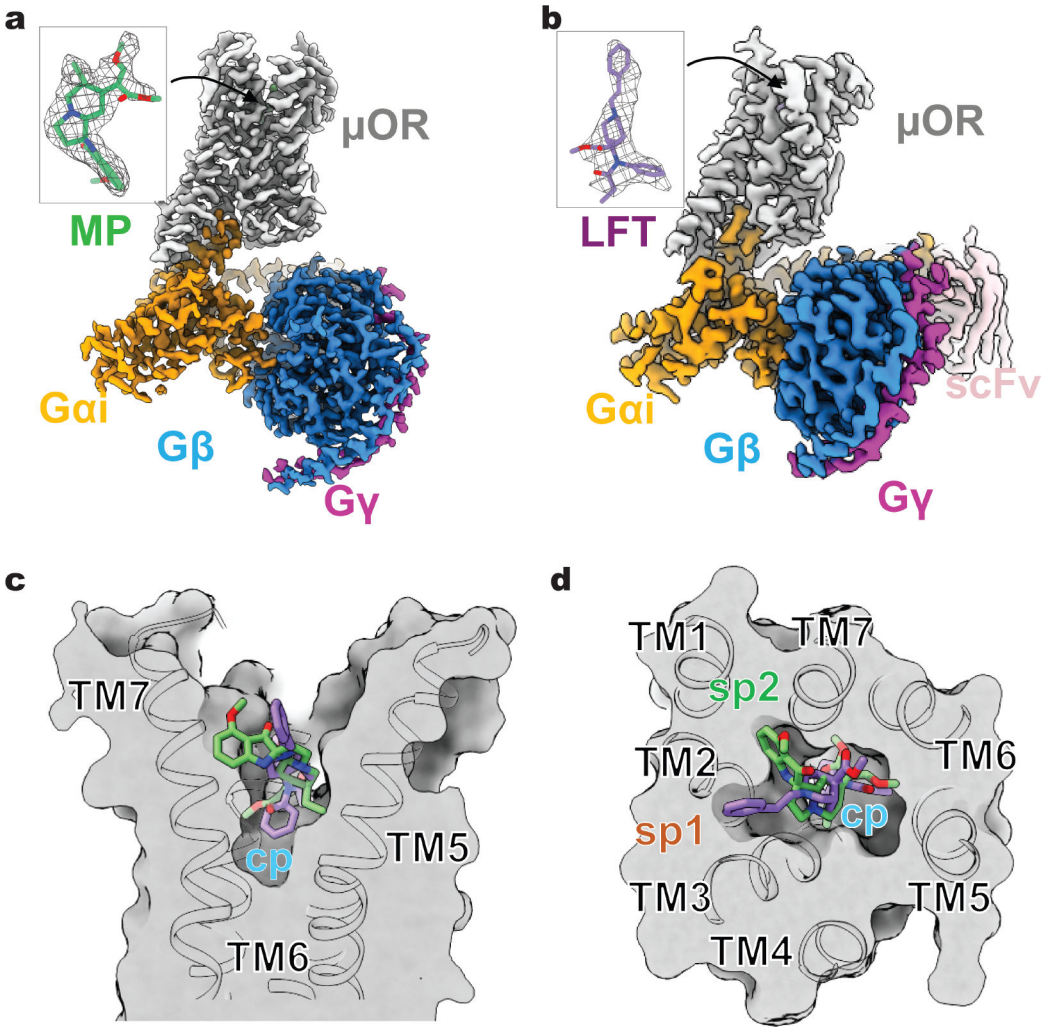

Fig. 2 |. Structures of μOR-Gi complex activated by MP and LFT.

a,b, 2.5Å cryo-EM map for the MP-μOR-Gi1 complex (**a**) and 3.2Å cryo-EM map for the LFT-μOR-Gi1-scFv complex (**b**). The insets highlight the well-resolved density (shown as wire-net) for MP (green) and LFT (purple). μOR is colored grey, Gαi1 in orange, Gβ in dodger blue, Gγ in magenta and scFv in pink. **c,d,** Superposition between the MP-μOR-Gi1 and LFT-μOR-Gi1-scFv structures shows that the structurally distinct MP and LFT occupy both a common central pocket (cp) in the orthosteric binding site (**c,** viewed from membrane plane, **d,** viewed from the extracellular side) while occupying different sub-pockets (sp1 and sp2).

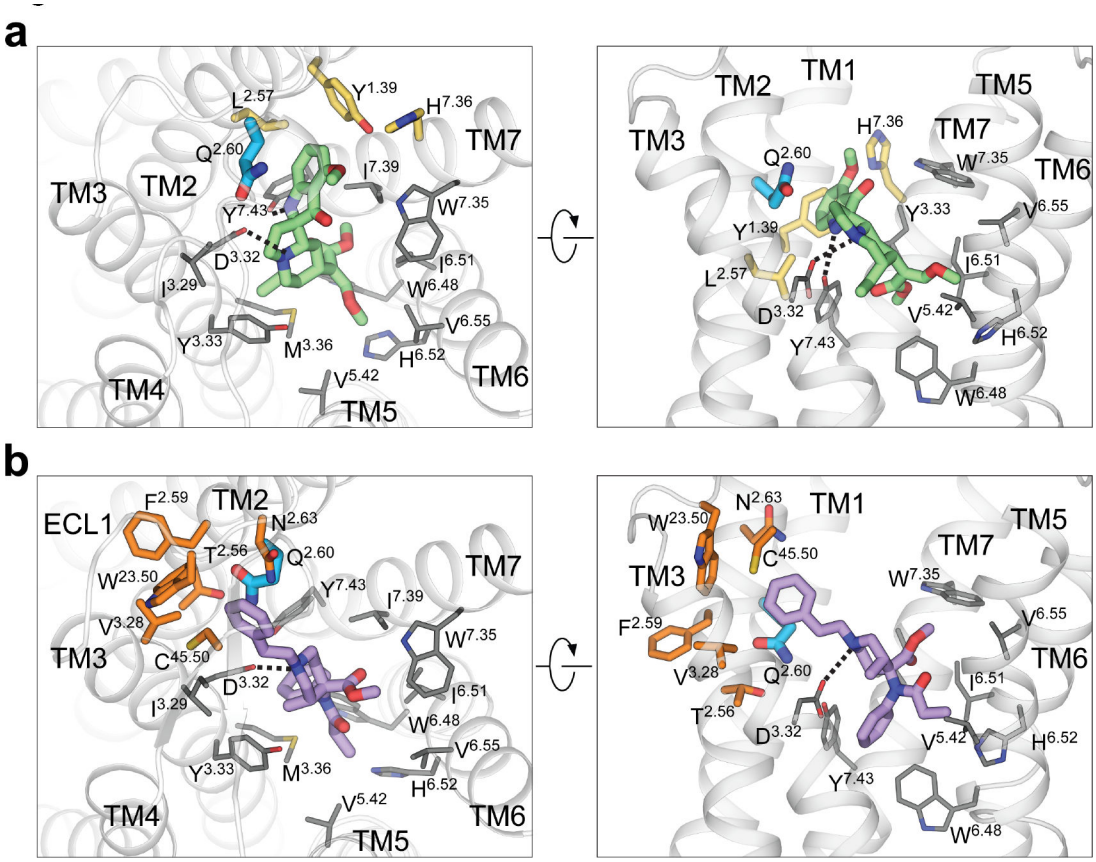

Fig. 3 |. Semi-conserved ligand interaction network for MP and LFT.

a,b, The μOR orthosteric binding pocket for MP (**a**) and LFT (**b**) viewed from the extracellular side (left panels) and membrane plane (right panels). Residues involved in both MP and LFT interaction are colored grey, while residues uniquely contributing to MP interaction are shown in yellow, and those for LFT in orange. Residue Q124$^{2.60}$, which interacts with both MP and LFT but in different orientations, is highlighted in blue. Dashed lines depict salt-bridge interactions.

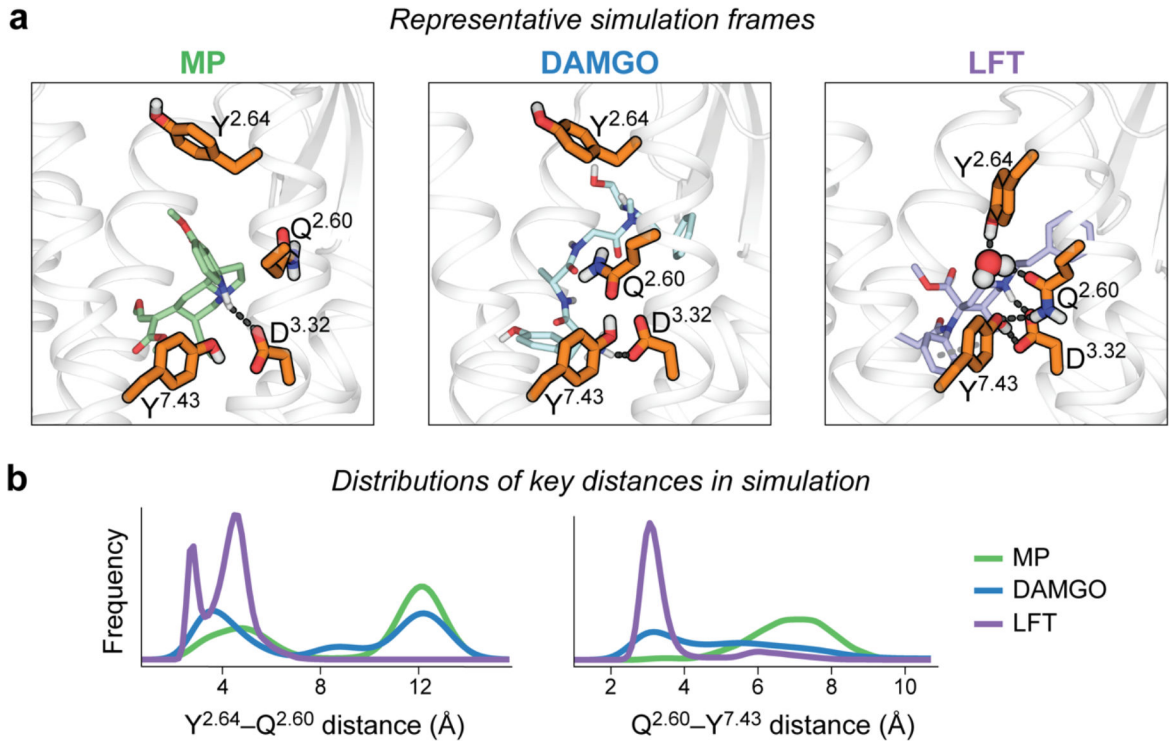

Fig. 4 |. Simulations of the μOR reveal distinct binding pocket conformations favored by MP, DAMGO, and LFT.

(a) Representative simulation frames showing ligand-specific hydrogen bonding networks in the binding pocket, involving key amino acid residues Y326$^{7.43}$, Q124$^{2.60}$, Y128$^{2.64}$, and D147$^{3.32}$ (see Methods). Black dashed lines represent hydrogen bonding interactions in the binding pocket, and the grey dashed line represents the **π–π** interaction between Y326$^{7.43}$ and the aniline group phenyl ring of LFT. The interaction between Y128$^{2.64}$ and Q124$^{2.60}$ is typically water-mediated. **(b)** Distributions of key inter-residue distances in simulations with various ligands bound. MP and LFT favor extreme conformations, whereas DAMGO samples a broader range of conformations, including the two extreme conformations favored by MP and LFT. Six independent simulations, each 3.5 μs in length, were performed for each ligand, without a bound G protein.

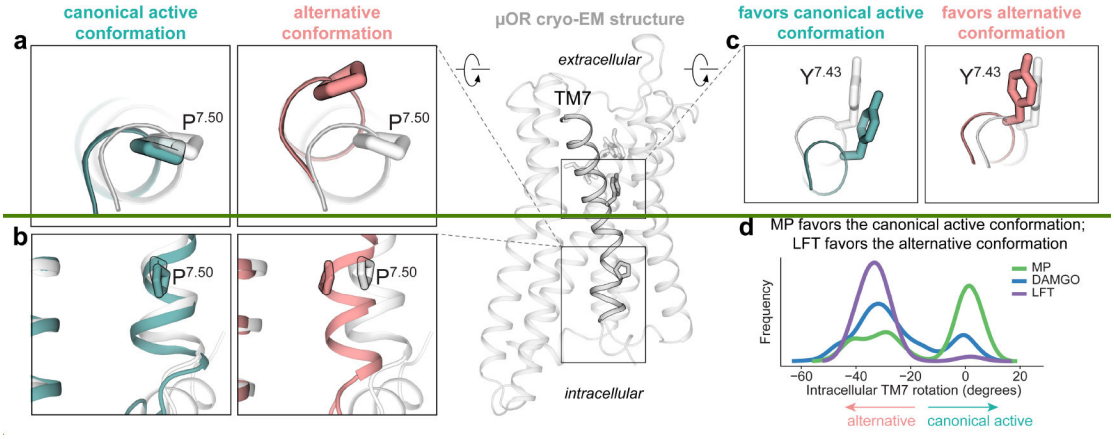

Fig. 5 |. In simulations with the G protein removed, the μOR adopts two active intracellular conformations, with MP and LFT favoring different conformations.

(a, b) At the intracellular coupling site, the canonical active conformation matches the intracellular conformation observed in the G protein–bound cryo-EM structures. The alternative active conformation is characterized by a counterclockwise twist at TM7 (when viewed from the extracellular side) and a resultant inward movement of P333$^{7.50}$. The grey rendering is based on the MP-μOR-Gi1 cryo-EM structure, but the TM7 structural features shown are essentially identical in the MP-μOR-Gi1, LFT-μOR-Gi1-scFv, and DAMGO-μOR-Gi1[31] cryo-EM structures. **(c)** A clockwise rotation of TM7 at the ligand binding site, specifically at Y326$^{7.43}$, favors the canonical active conformation, whereas a counterclockwise rotation favors the alternative state. **(d)** Relative to DAMGO, MP favors the canonical active conformation, whereas LFT favors the alternative conformation. The rotation of the intracellular portion of TM7 around its own axis is relative to the DAMGO-μOR-Gi1[31] cryo-EM structure (see Methods and Extended Data Fig. 7a). Negative values correspond to counterclockwise rotations, and positive values correspond to clockwise rotations.